

An analytical model for early-stage mooring design in floating wind turbines

Pierpaolo Loprieno ^{id a,b,*}, Fabio Rizzo ^{id b}, Elisa Leone ^{id c}, Dora Foti ^{id b},
Giuseppe Roberto Tomasicchio ^{id c}, Agostino Lauria ^{id c}

^a Department of Earth and Geoenvironmental Sciences, University of Bari Aldo Moro, Via E. Orabona, Bari, 70125, Puglia, Italy

^b Department of Architecture Construction and Design, Polytechnic University of Bari, Via E. Orabona, Bari, 70125, Puglia, Italy

^c Department of Engineering for Innovation, EUMER Campus Ecotekne, University of Salento, Via per Monteroni, Lecce, 73100, Puglia, Italy

ARTICLE INFO

Keywords:

Analytical modelling
Rigid-body mechanics
Dynamic behavior
Floating offshore wind turbine
Spar platform
Mooring system

ABSTRACT

The design of mooring systems for Floating Offshore Wind Turbines presents significant engineering challenges, particularly in managing structural dynamics and fluid-structure interactions. While analytical models are less developed in this sector compared to experimental and numerical approaches, they offer key advantages in streamlining early-stage design by reducing time, costs, and errors. This study proposes a novel Linearized Single Degree of Freedom analytical model to efficiently predict the dynamic response of spar-type Floating Offshore Wind Turbines under hydrodynamic loads. While Morison-based and linear mooring formulations are well established, in this work a closed-form solution is derived to accurately estimate translational displacements and mooring tensions. Implemented in MATLAB R2022a, the proposed model was validated against wave-tank experiments and subsequently compared with OpenFOAM and OpenFAST simulations to evaluate its accuracy levels. Despite its reduced formulation, the model accurately captures stiffness, damping, and hydrodynamic forces. Frequency- and time-domain analysis show strong agreement with experimental data, confirming its reliability in predicting platform displacements and mooring line tensions. It has also been demonstrated that the analytical model is able to yield precise results regarding both maximum and minimum values of these parameters, while effectively capturing their relationships. The model, with significantly lower computational demands than numerical simulations and comparable accuracy, serves as a valuable tool for early-stage design and optimization. While the proposed model is restricted to spar-type floating platforms under regular wave conditions, future work will aim to incorporate aerodynamic loads, irregular waves, and alternative platform configurations, without compromising computational efficiency.

1. Introduction

The current energy crisis has highlighted the need for the European Union (EU) to reduce its dependence on fossil fuels and diversify its energy supply, emphasising greener sources such as renewable energy. The EU, determined to lead the green transition to address the climate crisis, has set ambitious targets in the "Fit for55" package (Commission, 2021), including a 55% reduction in greenhouse gas emissions by 2030 and the achievement of climate neutrality by 2050. One of the main measures is the update of the "EU Renewable Energy Directive" (European Union, 2018), which aims to increase their share in the energy mix to 42.5%

* Corresponding author.

E-mail address: p.loprieno@phd.uniba.it (P. Loprieno).

Nomenclature

$O(x, y, z)$	cartesian reference system
i	i -th mooring line
n	number of mooring lines
q	number of harmonics
j	j -th harmonic
p	displacement field
t	time
ϵ	deformation field
$[M]$	mass matrix
$[C]$	damping matrix
$[K]$	stiffness matrix
$[I]$	identity matrix
$\{p(t)\}$	displacement vector
$\{\dot{p}(t)\}$	velocity vector
$\{\ddot{p}(t)\}$	acceleration vector
$p_{x,CP}(t)$	displacement of the structure at CP
$\dot{p}_{x,CP}(t)$	velocity of the structure at CP
$\ddot{p}_{x,CP}(t)$	acceleration of the structure at CP
$p_p(t)$	particular integral
$\{F(t)\}$	external forces vector
$F_{Morison}(t)$	Morison force
$F_{Inertia}(t)$	inertia force
$F_{FK}(t)$	Froude-Krylov force
$F_{Drag}(t)$	drag force
$F_{x,eq}(t)$	equivalent force
$\eta(t)$	free surface elevation
$u_x(z, t)$	horizontal velocity of wave particles
$\dot{u}_x(z, t)$	horizontal acceleration of wave particles
$u_x(t)$	resultant of the horizontal velocity
$\dot{u}_x(t)$	resultant of the horizontal acceleration
$F_{x,eq,0}$	mean value of force
$T_i(t)$	mooring line tension
T_a	analysis time considered
T	wave period
$C.I.$	initial conditions
FP_i	fairlead points
AP_i	anchor points
CP	centre of pressure
CM	centre of mass
E	Young's modulus
A	mooring line cross sectional area
$\alpha_i(t)$	horizontal angle of mooring line
$\beta_i(t)$	vertical angle of mooring line
$\epsilon_i(t)$	i -th mooring line deformations
$l_{0,i}$	mooring line unstretched length
$l_i(t)$	mooring line effective length
$l_{p,i}(t)$	horizontal plane projection of mooring
$l_{p,x,i}(t)$	x -axis projection of mooring length
$k_{El,i}$	mooring line elastic stiffness
$k_{G,i}(t)$	mooring line geometric stiffness
$k_{El,x,i}(t)$	x -axis projection of the mooring line elastic stiffness
$k_{G,x,i}(t)$	x -axis projection of the mooring line geometric stiffness
$k_{x,i}(t)$	x -axis projection of the mooring line overall stiffness
$k_{El,x}(t)$	x -axis projection of mooring system elastic stiffness
$k_{G,x}(t)$	x -axis projection of mooring system geometric stiffness
$k_x(t)$	x -axis projection of the mooring system overall stiffness
m_x	total mass of the structure
$m_{a,x}$	added mass

$m_{x,eq}$	equivalent mass
c_x	structural damping coefficient
$c_{q,x}(t)$	quadratic damping coefficient
$c_{x,eq}(t)$	equivalent damping
c_{cr}	critical damping coefficient
D	spar diameter
d	submerged height of the spar
H	wave height
h	seabed depth
g	gravity acceleration
κ	wave number
Ω	wave angular frequency
$\omega_d(t)$	damped pulsation of the structure
ω_n	natural pulsation surge
λ	wavelength
ρ	water density
β	decay parameter
$\zeta(t)$	damping factor
Φ	phase shift of wave
ϕ_j	phase shift of response
C_a	added mass coefficient
C_d	drag coefficient
C_m	inertia coefficient
C_1, C_2	constants
V_w	water volume displaced
A_w	wet area of the spar
a_j	sin Fourier coefficient
b_j	cos Fourier coefficient

by 2030, with a target of 45 %, as recommended by the "REPowerEU" plan (European Commission, 2022). Among the renewable energy sources, offshore wind resources in deep waters have gained increasing attention due to their high energy potential (Lauria et al., 2024a; Ricciardelli et al., 2021). Floating Offshore Wind Turbines (FOWTs) offer significant advantages over onshore and fixed-bottom offshore wind turbines in terms of energy generation potential and environmental impact (Afridi et al., 2024). These floating technologies enable the exploitation of vast marine areas, facilitating the installation of larger wind turbines with higher efficiency. Additionally, they allow access to stronger and more consistent wind speeds while mitigating visual and acoustic disturbances along the coast (Barooni et al., 2022). Despite their advantages, the large-scale deployment of FOWTs still faces several technical and economical challenges (Hong et al., 2024).

A structural element requiring particular attention is the mooring system (Lei et al., 2021). The mooring system plays a pivotal role in keeping FOWTs in place and ensuring their stability, providing structural safety and operational efficiency (Rui et al., 2024). Mooring lines, and therefore mooring systems, can be particularly vulnerable to failure, due to the complex framework arising from fluid-structure interaction, which can lead to failures in both the short and long term (Xu et al., 2023). The complexity of designing mooring systems, combined with the realistic possibility of damage over time, often results in the over-dimensioning of mooring lines. This approach significantly increases costs, not only for production but also for transportation, installation, and maintenance. These elevated costs significantly hinder the commercial success and broader implementation of such technologies (Hong et al., 2024). It has been demonstrated that the cost of fixing issues rises exponentially as a project moves from design to production and post-deployment stages. Early detection and resolution during the design phase are less costly and less disruptive (Patryniak et al., 2022), while later-stage problems, particularly after the product is released, can lead to significantly higher costs due to rework, recalls, and reputational damage (McMorland et al., 2022). This highlights the importance of early design reviews, testing, and quality assurance to prevent costly issues later on. In the context of FOWTs, optimizing the early design phases of mooring systems is a crucial strategy to enhance structural safety and ensure the commercial viability of these technologies (Ma et al., 2021).

Mooring systems are designed to restrict the movement of floating structures within specified design parameters by transferring loads from the floating platforms to the anchors. Consequently, the primary control parameters relevant to structural safety under the Ultimate Limit State (ULS) are the displacements of the floater and the tension induced in the mooring lines (DNV, 2021a, 2017, 2021b). While existing classification societies such as Det Norske Veritas (DNV), Bureau Veritas (BV) or American Bureau of Shipping (ABS) provide valuable formulations and design guidelines, the complexity of these structures, the challenging installation environments, and their dynamic interactions necessitate sophisticated complementary design supports, including experimental testing and advanced numerical modeling (Subbulakshmi et al., 2022). It is evident that both methodologies have been extensively employed

over time and are widely acknowledged as generally capable of capturing the dynamic behavior of FOWTs and their mooring systems. Nevertheless, both of them still present certain challenges regarding their applicability during the early stages of design. The experimental approach offers significant advantages in investigating the dynamic response of FOWTs and their mooring systems (Somoano et al., 2022; Lian et al., 2023; Liang et al., 2024) to various types of forcing through physical modeling, providing valuable insights (Subbulakshmi and Verma, 2024; Lin and Huang, 2022; Tang et al., 2023, 2025). Moreover, experimental data play a fundamental role in the development of Artificial Intelligence (AI) systems aimed at enhancing both the design phase (Medina-Manuel et al., 2024; Wang et al., 2025a; Wen et al., 2025) and the monitoring (Coraddu et al., 2024; Kumar et al., 2025; Sharma and Nava, 2024) of FOWTs, enabling high-accuracy failure prediction (Sasinthiran et al., 2024). However, despite the cruciality of experimental data, they often face challenges related to scaling laws and truncation techniques when adapting full-scale conditions to laboratory environments (ITTC, 2021a,c). These limitations can introduce discrepancies, requiring refined methodologies to account for scale effects accurately (Chen et al., 2020). Additionally, time and cost constraints, often coupled with limited test facilities and difficulty in identifying adequate measuring instruments, further hinder extensive physical testing especially in the early stages of the project (ITTC, 2021b). The utilisation of numerical models has thus emerged as a valuable tool for complementing and enhancing experimental investigations and various modeling approaches have been developed to accurately represent mooring systems (Zhong et al., 2024; Zhang et al., 2022; Martin and Bihs, 2021). These models must be employed within a multi-physics numerical simulation framework that integrates aero-hydro-servo-elastic interactions (Otter et al., 2022; Yu et al., 2023) to achieve a comprehensive representation of the dynamic response of FOWTs. Although significant advancements in numerical modeling (Zhang et al., 2024; Tang et al., 2024; Que et al., 2025; Wang et al., 2025b; Meng et al., 2025) have provided deeper insights into critical aspects (He et al., 2025; Lee and Lee, 2019; Kim et al., 2025; Li et al., 2024b; Bian et al., 2025; Lee et al., 2025) of FOWT mooring systems (Liu et al., 2024; Ali et al., 2025; Nie et al., 2024; Hao et al., 2025) and have been instrumental in improving mooring system design, Lozon et al. (2025), Neisi et al. (2024), Zhang et al. (2025), Coughlan et al. (2025), Zhang and Liu (2023), Xu et al. (2024), such models still exhibit intrinsic limitations that can lead to considerable challenges during the early design stages, thereby hindering the effective optimization of the overall design process. These methods require advanced techniques to capture the dynamic behavior of FOWTs and mooring system and, as the fidelity of the model increases, so does the complexity and uncertainty of the implementation, due to the numerous parameters that must be defined. Although several procedures have been developed to support these phases, such as the use of parametric models to efficiently identify optimal parameter sets for subsequent detailed numerical analysis (Uzunoglu and Soares, 2019), a considerable number of these parameters are often assumed and therefore require careful calibration and refinement through sensitivity analysis. In the preliminary design phase, however, the absence of prior knowledge of the structural response, often combined with the lack of experimental data for model validation, further complicates this process. The selection of these parameters exerts a significant influence on the accuracy of the predicted results. Consequently, it becomes necessary to increase the number of simulations to identify the most accurate values for these parameters and achieve an adequate level of model reliability and safety. This process is not only highly demanding in terms of time and cost but also introduces an inherent degree of uncertainty into the modeling process. Moreover, while high-fidelity simulations improve predictive accuracy, they entail significant computational costs, demanding substantial resources (Chen et al., 2020). This computational burden, both in terms of time complexity and data storage, can significantly constrain the initial design phases, where efficiency and flexibility are paramount.

Although analytical approaches remain far less explored than numerical and experimental methods, they could play a crucial role in addressing some of the limitations inherent to both. Analytical formulations, based on solid mathematical and physical principles, allow the estimation of key quantities without the substantial computational cost typically associated with high-fidelity simulations, both in terms of runtime and data storage, requiring significantly less effort to define and calibrate the necessary parameters. Furthermore, such models can be implemented efficiently in symbolic or analytical computation environments, as well as in any programming language, including open-source platforms (Lauria et al., 2024a). This flexibility significantly lowers both implementation effort and operational costs compared with experimental campaigns or commercial software. Although analytical models cannot replace advanced numerical or experimental techniques, their low computational requirements, rapid execution, ease of implementation, and flexibility make them an effective complement to these methods and particularly valuable in the early design process (Sablok et al., 2024). However, the development of fully analytical models with closed-form solutions that achieve high levels of accuracy remains extremely challenging due to the complex dynamics governing floating offshore wind systems. Most existing efforts focus on deriving analytical solutions for individual aspects or components relevant to the design of such structures. Several studies have attempted to develop and validate analytical formulations for accurately computing forces acting on FOWTs. For instance, Ronge et al. (2022) proposes a semi-analytical method that employs equations based on the formulations of Huang and Eatock Taylor to calculate second-order forces. Similarly, Gharechae and Negahdari (2022) introduces a semi-analytical approach to determine first-order horizontal forces induced by oblique waves. In Høeg and Zhang (2023), a semi-analytical hybrid model has been developed for computing hydrodynamic forces, allowing for simulations of FOWTs responses. Additionally, Borg and Collu (2015) describes a method for calculating hydrodynamic forces, approximating the radiation force and incorporating additional viscous resistance. Recent efforts have also focused on deriving analytical formulations for damping coefficients. For example, Meng et al. (2022) outlines an analytical procedure for defining both aerodynamic and hydrodynamic damping coefficients. In Yang et al. (2023), aerodynamic damping of a semi-submersible platform is examined using both a frequency-domain analytical method and a time-domain method based on fully coupled decay simulations. A semi-analytical solution for modal aerodynamic damping ratios is proposed in Xi et al. (2020). Moreover, Ishihara and Zhang (2019) presents correction factors for added mass and drag coefficients, analyzing their impact on global matrices. Structural deformability represents another critical area of investigation. In Al-Solihat and Nahon (2018), the floating platform, nacelle, and rotor are modeled as rigid bodies, while the wind turbine tower is treated as an elastic body. The hydroelastic effects of wave motion on a floating body are analyzed using a three-dimensional time-domain semi-analytical method

in Sengupta et al. (2017). Additionally, Hegseth and Bachynski (2019) employs a linear model with generalized displacements and a semi-analytical frequency-domain approach to establish the system's equations of motion. The analytical formulation of the stiffness matrix and mooring system dynamics has been extensively explored in the literature. For instance, Pesce et al. (2018) provides an explicit three Degrees of Freedom (DoF) analytical formulation for the stiffness matrix of a generic mooring system and Amaral et al. (2022) extends this to a six DoF mooring system. Instead, Amaral et al. (2024) presents a closed-form analytical formulation for the calculation of an equivalent stiffness of the mooring system with shared lines. A semi-analytical formulation for the static analysis of mooring lines, useful for their design and optimization, is presented in Dodaran and Park (2012). Furthermore, a quasi-static semi-analytical solution incorporating contact and friction with the seafloor is introduced in Masciola and Jonkman (2013). However, the current literature lacks a comprehensive exploration of purely analytical formulations with a closed-form solution capable of capturing the complex dynamic behaviors of FOWTs, including structural dynamics and mooring line tensions, which could enable more effective support and optimization of early-stage design.

The present study addresses the outlined context by proposing a novel Linearized Single-DoF (SDoF) analytical model for efficiently predicting the dynamic response of spar-type FOWTs caused by hydrodynamic loads. The model allows the derivation of a closed-form solution for evaluating the platform's translational displacements and mooring line tensions, providing adequate accuracy with minimal computational effort. The proposed analytical method is therefore particularly useful in the early design stages. It can be employed to perform parametric analysis, enabling a rapid and detailed assessment of how the platform's translational displacements and mooring line tensions vary with changes in the configuration and properties of the mooring system. This, in turn, enables a faster identification of the most suitable design solutions. Moreover, the method can support the validation of numerical models, reducing the uncertainty of numerical predictions and thereby enhancing the safety of the designed structures. It also provides valuable support in planning experimental campaigns, allowing a quick evaluation of whether the scale model accurately represents the full-scale system, thus minimizing uncertainties associated with scaling laws and mitigating the risk of costly errors and delays. In summary, by streamlining the early-stage design process and reducing uncertainties, thereby enhancing structural safety, this approach contributes to the overall optimization of mooring system design, a key factor in cost reduction, and consequently fosters the broader development of the floating offshore wind sector.

The remaining of the present paper is organized as follows: in Section 2 materials and methods employed are described; in particular the analytical model is introduced, detailing its assumptions and domain of applicability, then the experimental campaign is described, providing data used to validate the analytical model and finally two different numerical models used to compare results and evaluate the performance of the analytical approach are presented. The results are then discussed in Section 3 and finally conclusions are given in Section 4. Additional details and key insights of the analytical model can be found in Appendix A. A sensitivity analysis for one of the numerical models is provided in Appendix B.

2. Materials and methods

This section outlines the methodologies employed in this study. The analytical model (Section 2.1), which constitutes the foundation of the work, is presented first. Following this, the experimental campaign is described (Section 2.2), providing the data used to validate the model. Finally, both the numerical models are introduced (Section 2.3). Validated against the experimental data, these models not only serve to further corroborate the analytical approach but also offer valuable insights for performance comparisons.

2.1. Analytical model

In the present section, the analytical model is outlined, specifying the assumptions made and the boundaries of its applicability. The main aim of the present analytical model is to establish a formulation capable of predicting the tension in mooring lines of a spar-type FOWT when it experiences displacement due to wave action. Regardless of their material composition, mooring lines behave as cables, responding solely to tensile forces while remaining unaffected by compressive stresses. Variations in mooring line tension, defined as changes in tensile normal stress, are directly influenced by the deformation of the lines caused by the displacement of the buoyant structure at their attachment points, referred to as fairlead points (Zeng et al., 2022). Hydrodynamic loads induce a displacement field p of such structures. The dynamic displacement response of a structure subjected to external forces is governed by a second-order differential equation, a fundamental principle in structural dynamics. This equation characterizes the motion of the structure across all 6-DoF, as outlined below

$$[M]\{\ddot{p}(t)\} + [C]\{\dot{p}(t)\} + [K]\{p(t)\} = \{F(t)\}, \quad (1)$$

in which $[M]$, $[C]$, $[K]$, are the mass, damping and stiffness matrices respectively, $\{p(t)\}$, $\{\dot{p}(t)\}$, $\{\ddot{p}(t)\}$, are the displacement, velocity and acceleration vectors, whereas $\{F(t)\}$ is the vector of external forces.

Regardless of the complexity of the force system induced by wave action, it can always be represented by an equivalent unidirectional resultant force (DNV, 2021a). For spar-type FOWTs, the dominant displacement response occurs along this primary direction, which significantly influences mooring line tension. Consequently, this problem can be systematically addressed by analyzing the turbine's response exclusively in this direction using an equivalent SDoF model. Consider a spar-type FOWT held in place and stabilised by a generic mooring system. In the present analytical model, each mooring line is modeled as a straight element for any desired mooring system configuration. This assumption not only allows the consideration of taut mooring systems, but also enables the representation of catenary mooring systems through the definition of equivalent mooring configurations, suitably parameterized to approximate the

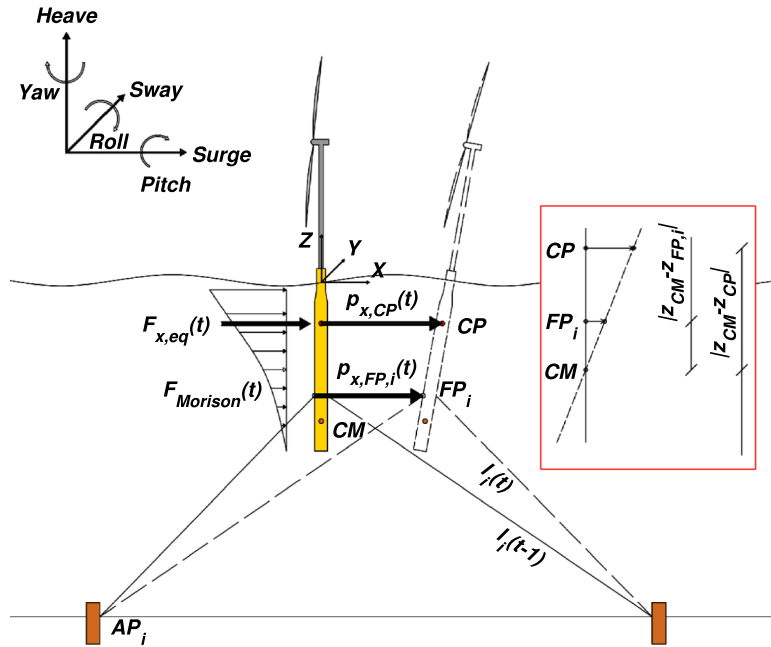


Fig. 1. Graphical representation of the hypotheses underlying the analytical model. Considering the Surge DoF parallel to the x-direction, the figure illustrates how the height-dependent Morison forces $F_{Morison}(t)$ are simplified into an equivalent force $F_{x,eq}(t)$ applied at CP. Assuming rigid body behavior and a fixed center of rotation at CM, the system undergoes rigid rotation, causing linear variation in displacements with height. Consequently, the displacement at FP_i is smaller than at CP, leading to variations in mooring line length and tension.

local stiffness of the actual catenary system within the small-displacement regime. Similar assumptions are commonly made in experimental campaigns, where truncated mooring setups are used to reproduce the full-scale restoring behaviour with good accuracy. From a modelling perspective, this choice will enable, in the subsequent Sub-Subsection, the derivation of a closed-form analytical formulation for the instantaneous tension of mooring lines, which can be directly evaluated without iterative procedures. Conversely, a classical catenary representation, although analytically defined through transcendental functions, does not admit a closed-form solution for tension as an explicit function of fairlead displacement. Consequently, using such a representation would have required iterative or numerical evaluations to determine the initial static pre-tensioning as well as to carry out the dynamic analysis. Furthermore, the adopted mooring model circumvents the piecewise functional dependence, which is imperative to consider transitions such as seabed contact and slack conditions, typical of conventional catenary models. The present assumption therefore reduces the complexity of the analysis, rendering it suitable for early-stage design and parametric studies within the normal operational regime. However, since it is only valid within the small-displacement regime, this assumption is not suitable for analyzing extreme events or highly nonlinear phenomena such as snap tension or slack conditions.

Referring only to the hydrodynamic loads, the deformations of the spar are negligible compared to the displacements, meaning that the displacement field is clearly greater than the deformation field $p \gg \epsilon$. Considering also that the connection between the superstructure and the floating structure can be regarded as perfectly fixed, the entire system (floater-tower-rotor-nacelle) may be regarded as a rigid body. A reference system, designated $O(x, y, z)$, is established with its origin at the axis of the FOWT, situated at sea level. Consider a horizontal-axis turbine oriented such that the rotor's axis of rotation is aligned with the x-axis. Assuming that the wave motion acts parallel to the x-axis, the DoF under evaluation is the horizontal translational surge. To isolate this DoF it is assumed that the turbine has reached equilibrium with respect to all other DoF and maintains this equilibrium over time. Although in real applications it is practically impossible to completely eliminate other oscillations, many designs of FOWTs aim to keep the hub height constant by ensuring buoyancy neutrality by various methods (Li et al., 2024a; Aboutalebi et al., 2024). The assumptions presented are clarified in Fig. 1.

The presentation of the analytical model is organized as follows. Section 2.1.1 will introduce the key structural characteristics, with a particular emphasis on the calculation of structural stiffness, simplifying the problem to a SDoF system. In Section 2.1.2, the linearization procedure will be discussed, culminating in the formulation of the SDoF equation of motion. Finally, Section 2.1.3 will define the time-dependent solution of the equation of motion and explore its relationship with the variation in tension within the mooring lines.

2.1.1. Equivalent structural stiffness calculation

Let's now proceed to the identification of the equivalent mass, damping and stiffness values to be used in the SDoF system to be analysed. It is acknowledged that, in general, the mass matrix of a floating structure is a full 6×6 matrix, including coupling terms between translational and rotational DoF. However, with the aim of analysing a SDoF model with respect to a translational DoF, the

system is assumed to be fully decoupled, and the mass matrix can be considered diagonal and expressed as $[M] = M[I]$, where $[I]$ is the identity matrix. Accordingly, irrespective of the DoF under consideration, the mass value remains constant. Let's then denote with m_x the total mass of the structure, where the subscript x , from now on, is representative of the DoF under consideration. $[C]$ is not a diagonal matrix, but is generally assumed to be diagonalisable. In fact, for real structures, the structural damping capacity is generally assumed to be a single value regardless of the DoF considered. Let's hence denote by c_x the structural damping coefficient of the FOWT considered. The stiffness of a structure reflects its ability to resist displacements caused by external forces. Based on the assumptions outlined, the mooring system is the sole contributor to the overall stiffness (Ullah et al., 2021). It is therefore necessary to determine the stiffness contribution provided by the mooring system in the x -direction when the structure experiences displacement along the surge DoF, considering that for a generic mooring system, mooring lines have two inclinations (Yang et al., 2022), one in the horizontal plane and one in the vertical plane. Mooring lines primarily operate in tension, making axial stiffness the dominant factor, while bending stiffness remains negligible. The stiffness of the i -th mooring line arises from two distinct components (Al-Solihat and Nahon, 2016),

$$k_{El,i} = EA / l_{0,i}, \quad k_{G,i}(t) = T_i(t) / l_i(t). \tag{2}$$

The first contribution $k_{El,i}$ is related to the geometric and material characteristics of the mooring line, defined as elastic stiffness where E is the Young's modulus of the material employed, A is the cross sectional area of the mooring line and $l_{0,i}$ is its unstretched length. The second contribution $k_{G,i}(t)$, defined as geometric stiffness, is related to the tension experienced by the cable in its configuration, where $T_i(t)$ is the mooring line tension in correspondance of the fairlead points and $l_i(t)$ is its length, considering the instant t . At the equilibrium position, $t = 0$, the cables may already be subjected to an initial tension or pretension, meaning they could already be in a deformed configuration. It should be noted that, in accordance with the displacements experienced by the structure, the geometric configuration of the mooring lines will change, and consequently, their tension will also vary. It therefore follows that the geometric stiffness of the mooring lines is a time-dependent quantity. Denoting by n the number of mooring lines that compose the mooring system, similarly to the SDOF spring-mass-spring systems, the contribution of the overall elastic and geometric stiffness of the system (Pesce et al., 2018) in the considered x DoF are obtained respectively as

$$k_{El,x}(t) = \sum_{i=1}^n k_{El,x,i}(t), \quad k_{G,x}(t) = \sum_{i=1}^n k_{G,x,i}(t). \tag{3}$$

Note that, although the elastic axial stiffness $k_{El,i}$ of the mooring line is constant because refers to an undeformed condition of the cable $l_{0,i}$ that is independent of time, its contribution $k_{El,x,i}(t)$ along the x -axis will vary over time in accordance with the changing configuration of the mooring system due to the displacements it undergoes. The overall stiffness of the mooring system, considering only the affecting contribution for the DoF examined, will therefore be the sum of the elastic and geometric stiffnesses of each mooring line

$$k_x(t) = k_{El,x}(t) + k_{G,x}(t). \tag{4}$$

Further analytical details on the calculation of the individual stiffness contributions $k_{El,x,i}(t)$ and $k_{G,x,i}(t)$ of the mooring lines are provided in A.1.

2.1.2. Problem linearisation and SDOF equation of motion

For the general application of spar-type FOWTs, the assumption of deep-water conditions is appropriate, defined as $h > \lambda / 2$, where h represents the seabed depth and λ is the wavelength. Typically, the use of a spar-type floating structure in deep water satisfies the condition $D \ll \lambda$, where D denotes the spar diameter. Under this assumption, the interaction between the fluid and the structure does not significantly alter the water flow, rendering diffraction effects negligible. Consequently, the Morison force ($F_{Morison}(t)$) can be employed to describe the hydrodynamic load ($F_x(t)$), specifically using its relative-velocity formulation for a moving body in oscillatory flow (Haritos, 2007). Therefore, it is possible to use Morison's equation to obtain the resultant of the hydrodynamic loads acting on the structure under consideration, which will be applied in the centre of pressure CP (calculation is presented in A.2). The Morison force is comprised of three distinct components. Let's therefore define $p_{x,CP}(t)$, $\dot{p}_{x,CP}(t) = \partial p_{x,CP}(t) / \partial t$, $\ddot{p}_{x,CP}(t) = \partial^2 p_{x,CP}(t) / \partial t^2$, respectively displacement, velocity and acceleration of the structure at CP , and $u_x(t)$, $\dot{u}_x(t)$ the resultant of the velocity and acceleration of the wave particles in the horizontal direction, obtained by integrating over the entire submerged height of the spar d their effective distribution $u_x(z, t)$, $\dot{u}_x(z, t)$ along the z -axis (defined in A.2)

$$u_x(t) = \int_{-d}^0 u_x(z, t) \, dz, \quad \dot{u}_x(t) = \int_{-d}^0 \dot{u}_x(z, t) \, dz. \tag{5}$$

Noted that C_a is the added mass coefficient, C_d is the drag coefficient and $C_m = C_a + 1$ is the inertia coefficient, denoting A_w the wet area of the spar, with reference to the section perpendicular to the direction of the flow, V_w the water volume displaced by the spar, and ρ the water density, the hydrodynamic load can be defined as

$$F_x(t) = F_{Morison}(t) = F_{Inertia}(t) + F_{FK}(t) + F_{Drag}(t), \tag{6}$$

where $F_{Inertia}(t)$ is the inertia force which is expressed as

$$F_{Inertia}(t) = \rho C_a V_w (\dot{u}_x(t) - \ddot{p}_{x,CP}(t)), \tag{7}$$

$F_{FK}(t)$ is the Froude-Krylov force expressed as

$$F_{FK}(t) = \rho V_w \dot{u}_x(t), \quad (8)$$

$F_{Drag}(t)$ is the drag force expressed as

$$F_{Drag}(t) = \frac{1}{2} \rho C_d A_w (u_x(t) - \dot{p}_{x,CP}(t)) |u_x(t) - \dot{p}_{x,CP}(t)|. \quad (9)$$

It should be noted that Eq. (9) has a highly non-linear form. However, for applications on real structures, when $\dot{p}_{x,CP}(t) \ll u_x(t)$ (Haritos, 2007; Merz et al., 2009; Santo et al., 2018) the degree of non-linearity of the drag force can be reduced by approximating it as

$$F_{Drag}(t) \approx \frac{1}{2} \rho C_d A_w [u_x(t) |u_x(t)| - 2 |u_x(t)| \dot{p}_{x,CP}(t)]. \quad (10)$$

Defining the added mass as $m_{a,x} = \rho C_a V_w$ and the quadratic damping coefficient as $c_{q,x}(t) = \rho C_d A_w |u_x(t)|$ (Malta et al., 2010), and introducing the equivalent mass terms of the system $m_{x,eq} = m_x + m_{a,x}$ and the equivalent system damping $c_{x,eq}(t) = c_x + c_{q,x}(t)$ it is possible to reorder the various factors in the equation of motion (detailed are outlined in A.3) and obtain at the second member an equivalent force $F_{x,eq}(t)$ which now has the classical form of the Morison equation

$$F_{x,eq}(t) = \rho C_m V_w \dot{u}_x(t) + \frac{1}{2} \rho C_d A_w u_x(t) |u_x(t)|. \quad (11)$$

Eq. (11) has a periodic, non-harmonic and still non-linear form related to the product $u_x(z, t) |u_x(z, t)|$, so Fourier series expansion can be employed to linearize the problem by decomposing the periodic forcing into a sum of harmonic components. Assuming q to be the number of harmonics considered and using the subscript j to denote the j -th harmonic, it is possible to rewrite Eq. (11) as

$$F_{x,eq}(t) = F_{x,eq,0} + \sum_{j=1}^q a_j \sin(j\Omega t) + \sum_{j=1}^q b_j \cos(j\Omega t), \quad (12)$$

in which

$$F_{x,eq,0} = \frac{1}{T} \int_0^T F_{x,eq}(t) dt \simeq 0, \quad a_j = \frac{2}{T} \int_0^T F_{x,eq}(t) \sin(j\Omega t) dt, \quad b_j = \frac{2}{T} \int_0^T F_{x,eq}(t) \cos(j\Omega t) dt. \quad (13)$$

It is now possible to define the final form of the second-order differential equation capable of describing the dynamic behaviour in the DoF surge of a spar-type FOWT with the defined mooring system subjected to hydrodynamic loads

$$m_{x,eq} \ddot{p}_{x,CP}(t) + c_{x,eq}(t) \dot{p}_{x,CP}(t) + k_x(t) p_{x,CP}(t) = F_{x,eq,0} + \sum_{j=1}^q a_j \sin(j\Omega t) + \sum_{j=1}^q b_j \cos(j\Omega t). \quad (14)$$

2.1.3. Time-dependent solution and mooring line tension

The time-dependent solution of Eq. (14) is described by the following expression

$$p_{x,CP}(t) = e^{(-\beta t)} [C_1 \sin(\omega_d(0)t) + C_2 \cos(\omega_d(0)t)] + \sum_{j=1}^q p_j^{(a_j)}(t) + \sum_{j=1}^q p_j^{(b_j)}(t). \quad (15)$$

In such a solution, $e^{(-\beta t)}$, with

$$\beta = c_{x,eq}(0) / 2m_{x,eq}, \quad (16)$$

represents the decay function of the oscillations due to damping; it should be noted that this parameter refers to structural damping and is therefore considered constant over time. For this reason is used the value at $t = 0$ of $c_{x,eq}(t)$, where the quadratic damping component is absent. $\omega_d(t)$ represents the oscillation frequency, or rather the damped pulsation of the structure in the DoF surge and is expressed as

$$\omega_d(t) = \omega_n \sqrt{1 - \zeta^2(t)}. \quad (17)$$

For the transitional phase is considered $\omega_d(0)$ as it is structure-related only and therefore excludes the contribution of the quadratic damping. Note that ω_n , representing the natural pulsation surge is expressed as

$$\omega_n = \sqrt{k_{El,x}(0) / m_{x,eq}}, \quad (18)$$

and only includes the elastic stiffness of the system as it is related to the intrinsic characteristics of the structure (Lee et al., 2024), so it does not depend on the time. For this reason, only the initial condition of elastic stiffness is to be considered. $\zeta(t)$ is the damping factor described as

$$\zeta(t) = c_{x,eq}(t) / c_{cr}, \quad (19)$$

which expresses the ratio between the damping coefficient and the critical damping coefficient c_{cr} , equal to

$$c_{cr} = 2\sqrt{k_{El,x}(0)m_{x,eq}}, \quad (20)$$

which is determined by the initial stiffness properties and remains constant over time, similar to the natural frequency of oscillation. The constants C_1 and C_2 of Eq. (15) are determined based on the initial conditions $C.I.$ of the problem. The reader is invited to refer to the A.3 for detailed explanations of the calculation of the C_1 and C_2 constants employed in the present study, taking into account the null $C.I.$.

Having identified and defined the SDoF equation of motion for the surge DoF relative to CP , the aim is to evaluate how this displacement induces deformation in the mooring lines, leading to a variation in tension. It is important to note that, to ensure buoyancy, the center of mass CM of such structures is positioned lower than the geometric centroid and thus lies significantly below the CP . In typical configurations of spar-type FOWT, the mooring lines fairlead points, FP_i , are located below CP and closer to CM (Jonkman, 2010; DNV, 2021b). Let's consider that the structure's mass and inertia properties can be assumed to be concentrated at CM , which maintains a constant position within the body over time, with no vertical or horizontal displacement relative to the body itself, and that the hydrodynamic loads can be assumed to act at CP . The hydrodynamic loads cause horizontal translation of the structure and under the rigid body assumption made earlier, with reference to the global reference system, the CM moves rigidly with the structure only in the horizontal direction, and it is also induced a rigid rotation around the CM (Goupee et al., 2014), consistent with the pitch DoF, resulting in a linear variation of displacements along the height of the structure. A graphical representation is provided in Fig. 1. Based on these considerations, by applying a linear variation law for displacements along the height, it is possible to derive the horizontal displacements in the surge direction at various points FP_i starting from the horizontal displacements calculated at CP with the SDoF model:

$$p_{x,FP_i}(t) = p_{x,CP}(t) |z_{CM} - z_{FP_i}| / |z_{CM} - z_{CP}|. \quad (21)$$

The time-dependent solution for the different FP_i (Eq. (21)) enables the calculation of displacements in the surge direction and consequently evaluate the deformations ε_i undergone by the different mooring lines. From simple geometric considerations delineated in A.4, as were employed for the equivalent stiffness calculation, in relation to the assumptions underlying this numerical model, deformed length of the mooring lines $l_i(t)$ can be obtained, instant by instant. Therefore, it is now possible to calculate for each mooring line the tension $T_i(t)$ over time as

$$T_i(t) = EA\varepsilon_i(t) = EA[(l_i(t) - l_{0,i}) / l_{0,i}]. \quad (22)$$

This value represents the tension at the fairlead point. When studying the dynamic behaviour of the platform, the most influential and limiting factor affecting the structure's movements is the resultant force applied to the fairlead. It is indeed through this point that the mooring line transmits reactions to the platform in response to environmental loads. Under standard operating conditions, the tension at the fairlead generally represents the maximum value along the mooring line (Jiang, 2025). Therefore, analysing it provides a useful and generally conservative indication of cable tension levels. A graphical representation of the key hypotheses and assumptions underlying the analytical model is presented in Fig. 1.

Although this work has been developed with reference to the surge DoF, it should be noted that, by considering waves acting along the y -axis together with the corresponding mooring system stiffness components in the same direction, the translational sway displacement and the resulting mooring tensions can similarly be assessed.

2.2. Experimental campaign

This section outlines the key features of the experimental campaign, from which the data were obtained and against which the analytical model was compared and validated. In this section we report on the information from the experimental campaign, focusing on the information relevant to the present work. Additional detailed information on other aspects can be found in Lauria et al. (2024b).

The dataset for this study originates from experimental tests at the DHI Offshore Wave Basin in Hørsholm, Denmark, conducted as part of the Hydralab EU-funded project, already presented in Tomasicchio et al. (2020), Russo et al. (2021). The setup provides comprehensive data for analyzing wave-structure interactions in controlled deep-water conditions.

Key details include:

- wave basin specifications: the basin measures 20 m x 30 m, with a depth of 3 m; a central pit (3 m x 3 m, depth 6 m) was used to simulate deep-water conditions;
- wave generation: a wave generator with 60 individually controlled 1.5 m flaps produces regular, irregular, directional, and unidirectional waves; a 6.5 m wave absorber minimizes reflections;
- measurement setup: nine wave gauges (three in front, six behind) measure free surface elevation (FSE) along the wave direction; a non-contact optical tracking system and three accelerometers monitor 6-DoF motion of the FOWT; a strain gauge load cell (300 N capacity) measures tension in the mooring line.

The FOWT that has been subjected to analysis is a Froude 1 : 40 scale model. The structure comprises a floating spar-type substructure, scaled from the Phase IV prototype of the OC3-Hywind project (Jonkman, 2010) with a three-line non-redundant catenary mooring system, while the wind turbine itself is a scaled representation of the NREL 5 MW turbine (Jonkman, 2009). Given the limited depth of the wave basin, it was necessary to employ a truncation method for the mooring system. The mooring system comprises three lines arranged in a triangular configuration, spaced 120 degrees apart. Two lines are positioned in front of the model and one behind, relative to the direction of wave action. Each mooring line consists of a series of seven steel helical springs assembled in sequence.

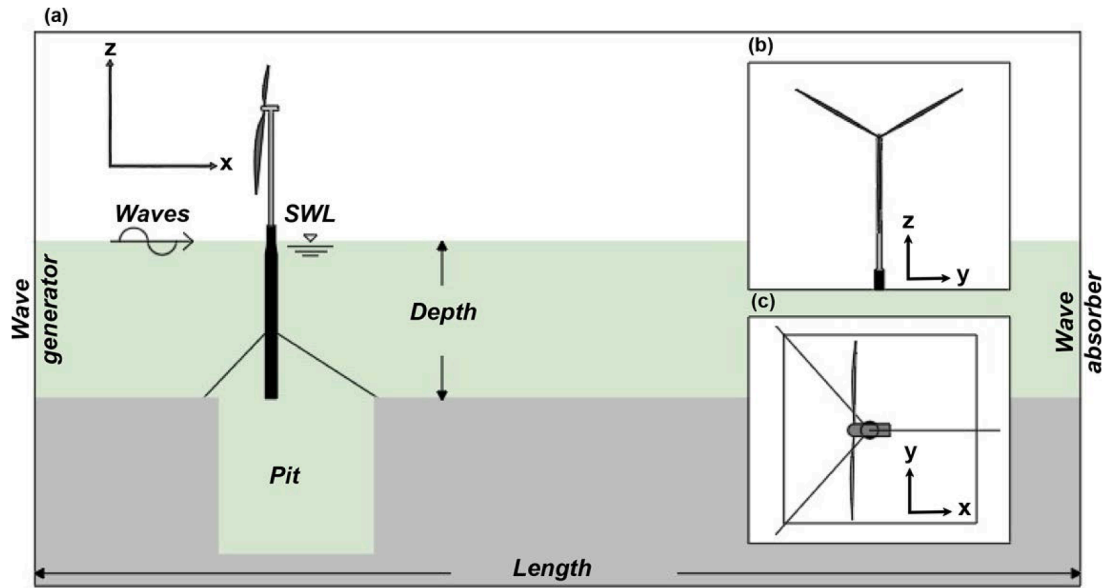


Fig. 2. Schematic representation of the experimental setup: (a) positioning of the scaled model within the test basin, aligned with its longitudinal dimension and centered over the deep-water pit; the wave propagation direction, from the generator to the absorber along the x-axis, is also indicated; (b) front view of the rotor, allowing a comparison with (a) to infer the blade positioning during the test; (c) top view of the model above the deep-water pit; comparing (a) and (c) provides insight into the mooring system configuration during the experiment.

Table 1

Main features of the 1:40 Froude-scaled model of a spar-type floating offshore wind turbine tested during the experimental campaign. Specifically, the wind turbine characteristics are presented first, followed by the floating platform and, finally, the mooring system.

	Properties	Units	Value
Wind Turbine	Rotor diameter	<i>m</i>	3.15
	Hub diameter	<i>m</i>	0.0075
	Tower diameter	<i>m</i>	0.08
	Elevation to tower base above SWL	<i>m</i>	0.25
	Elevation to tower top above SWL	<i>m</i>	2.19
	Hub height	<i>m</i>	2.25
	Rotor mass	<i>kg</i>	1.72
	Nacelle mass	<i>kg</i>	3.75
Floating Platform	Diameter upper cylinder	<i>m</i>	0.163
	Diameter lower cylinder	<i>m</i>	0.235
	Total draft	<i>m</i>	3
	Center of gravity below SWL	<i>m</i>	2.25
	Mass including ballast	<i>kg</i>	116.66
	Roll inertia	<i>kg · m²</i>	41.3
	Pitch inertia	<i>kg · m²</i>	41.3
	Yaw inertia	<i>kg · m²</i>	1.6
Mooring System	Elevation to platform top above SWL	<i>m</i>	0.3
	Number of mooring lines	-	3
	Horizontal angle	°	120
	Depth to anchors below SWL	<i>m</i>	3
	Depth to fairleads below SWL	<i>m</i>	1.75
	Radius to anchors from platform centerline	<i>m</i>	2.05
	Unstretched mooring length	<i>m</i>	1.79
	Stretched mooring length	<i>m</i>	2.25
	Equivalent springs extensional stiffness	<i>N/m</i>	27.25
Linear mass density	<i>kg/m</i>	0.047	

Prior to installation, the springs were individually weighed and tested in tension to determine their linear mass density and elastic stiffness, which were then used to select and combine the springs appropriately for each line. Each line has a linear mass density of 0.047 kg/m and an axial stiffness of 48.77 N, corresponding to 27.25 N/m. The unstretched length of each line is 1.79 m, while the maximum stretched length is 2.25 m. The mooring lines are connected to the spar via a collar located 1.75 m below the still water level and anchored at a depth of 3 m with a horizontal distance of 2.05 m from the platform centerline. This configuration was designed to reproduce, in Froude scale, the same surge-sway stiffness and overall restoring behaviour of the OC3-Hywind project mooring system, while maintaining the correct position of the center of gravity. The truncated setup therefore ensures dynamic similarity between the experimental and full-scale configurations. Further information can be found in Fig. 2 and Table 1. Experimental aspects concerning the aerodynamic components have been deliberately excluded, as they lie beyond the scope of the present study.

2.3. Numerical methods

In order to model the dynamic behaviour of the investigated spar-type FOWT, two numerical models were implemented based on two distinct approaches, carefully selected as representative of the state-of-art in the floating offshore wind industry. This better contextualizes the proposed analytical model relative to established benchmarks, highlighting its role as an early-stage, complementary tool rather than as a substitute for high-fidelity codes.

A numerical model was defined in OpenFOAM, an open-source CFD solver, using Reynold-Averaged Navier-Stokes (RANS) equations to represent the behaviour of the floating body, coupled with MoorDyn (Chen and Hall, 2022), a solver for the dynamic behaviour of mooring lines. A second numerical model was developed using OpenFAST, an open-source simulation framework developed by National Renewable Energy Laboratory (NREL) for the coupled aero-hydro-servo-elastic analysis of onshore and floating offshore wind turbine systems. In this model, the mooring lines were modeled through MAP++, which is interfaced with OpenFAST and provides a quasi-static formulation for simulating the dynamics of mooring systems.

This section presents the key aspects of the numerical models, which are validated against the experimental data outlined in Section 2.2 and employed to compare results and assess the performance of the analytical approach. The Subsection is structured as follows. Section 2.3.1 is dedicated to the description of the OpenFOAM numerical model: Paragraph 2.3.1.1 describes the multiphase computational fluid dynamics solver used and the modeling of fluid-structure interaction; Paragraph 2.3.1.2 details the external solver employed for mooring system modeling and its coupling with the multiphase solver; finally, Paragraph 2.3.1.3 provides an overview of the computational domain, mesh settings, and prescribed boundary conditions. Section 2.3.2, on the other hand, is dedicated to the description of the OpenFAST numerical model.

2.3.1. OpenFOAM numerical model

2.3.1.1. Numerical multiphase solvers. It was opted for olaFlow, an OpenFOAM-based solver specifically developed to simulate wave generation, propagation, and absorption, making it particularly useful for coastal and offshore engineering applications. Unlike interFoam, which is a general-purpose two-phase solver, olaFlow includes advanced boundary conditions that enable realistic wave modeling and more accurate studies of wave-structure interactions. The RANS described for the two incompressible fluids, is solved using the Volume of Fluid (VOF) method, which captures the free surface and the finite-volume discretization method. The governing equations are based on the two fundamental equations of conservation of mass and momentum for an incompressible and viscous fluid. The Boussinesq approximation was used to close the system. The kinematic eddy-viscosity has been expressed as a function of the turbulent kinetic energy k and the dissipation rate ω , leading to a ‘two-equation’ turbulence model. Two-equation models provide, as the name suggest, two equations: the former equation is used to compute the turbulent kinetic energy per unit mass k and the latter equation is needed to calculate a specific dissipation rate ω . This model is complete to predict properties of a given turbulent flow without prior knowledge of the turbulence structure. In this paper the $k - \omega$ SST model proposed by Menter is used to define a relationship between the Reynolds stresses and the mean flow field, solving the closure problem. The $k - \omega$ SST turbulence model selected show several relatively minor variations from the original SST version (Lauria and Alfonsi, 2020).

Wave generation and absorption were carried out using the OlaFlow toolbox, with both boundaries defined as static, i.e., without the use of moving paddles or relaxation zones. Wave generation was imposed through a first-order Stokes wave model (Dean and Dalrymple, 1991), with a wave angle fixed at 0°. The generation boundary condition prescribes both the velocity field and the volume fraction to introduce the desired wave train into the computational domain. Wave absorption was implemented at the opposite boundary using the quasi-3D active absorption method proposed by Schäffer and Klopman (2000). This approach dynamically modifies the outflow conditions to enable outgoing waves to exit the domain while minimizing reflection. By defining the incident wave angle a priori, the method avoids the need for real-time directional analysis and enables efficient absorption of wave energy. This helps mitigate mean water level variations caused by the mass imbalance between wave crests and troughs when no absorbing condition is applied. In order to simulate buoyancy and accurately capture the dynamic behaviour of the structure under investigation for all 6-DoF, the sixDoFRigidBodyMotion library was applied. In this library, the equations of motion are formulated on the basis of the linear and angular momentum conservation laws. The Newmark integration scheme is applied to guarantee, instantaneously, the values of velocity, position and orientation of the floating body, given the external forces acting on the body (Chen and Hall, 2022).

2.3.1.2. Mooring dynamic model and coupling with OpenFOAM. The modelling of the mooring lines was conducted using the dynamic solver MoorDyn. The solver is based on the concentrated mass model, which discretises the mooring lines into a series of segments that behave like massless springs. At the vertices of these segments, masses, external forces and inertia reactions are concentrated.

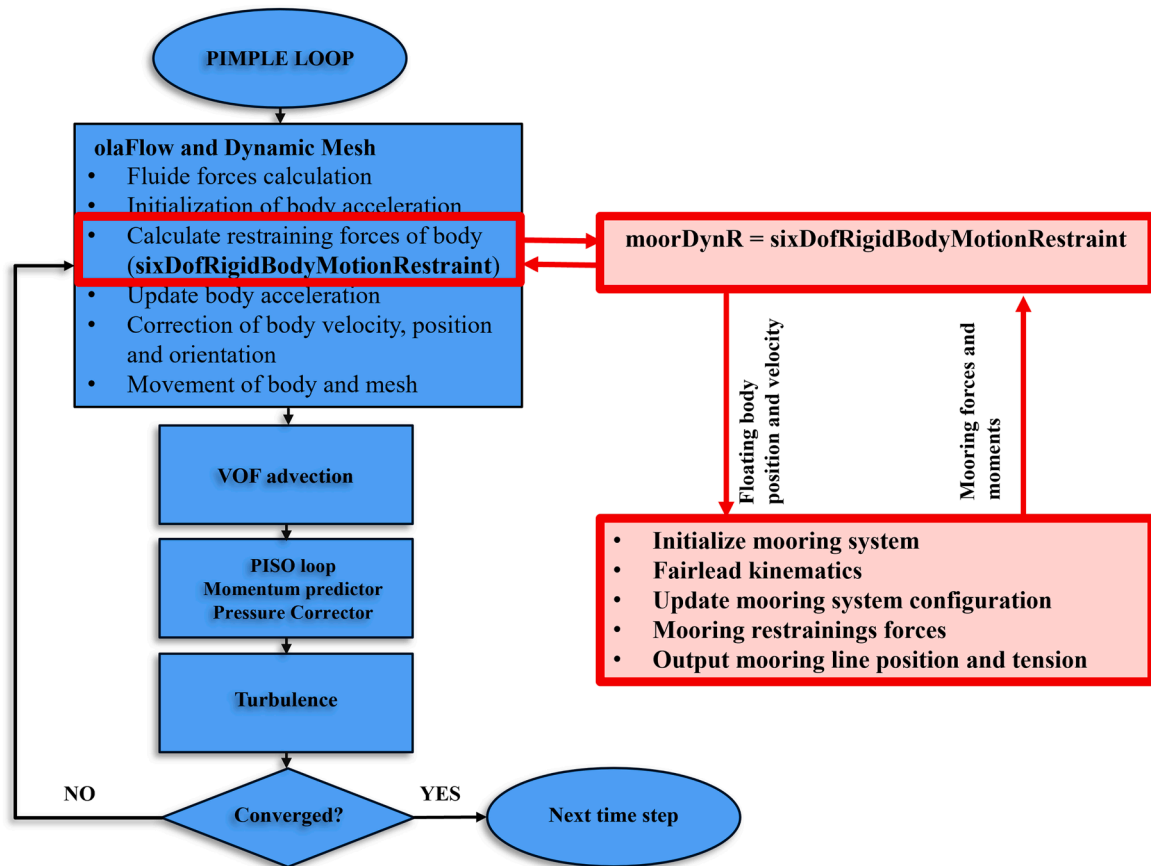


Fig. 3. Algorithm used for the coupling between OpenFOAM and MoorDyn (adapted from [Chen and Hall \(2022\)](#)). The coupling of floating body motion with free surface flow is achieved using a PIMPLE loop, combining SIMPLE and PISO algorithms. MoorDyn is loosely coupled with the body motion solver to compute mooring forces and update body acceleration. Multiple PIMPLE iterations may be needed for convergence. More details on the coupling methodology can be found in [Chen and Hall \(2022\)](#).

The mooring lines are described through their diameter, unstretched length, density and internal and external forces acting on each of the nodes ([Chen and Hall, 2022](#); [Aliyar et al., 2022](#); [Jiang et al., 2020](#)).

The PIMPLE loop, shown in [Fig. 3](#), serves as the foundational algorithm for simulating the coupled dynamics of a floating body and its mooring lines ([Chen and Hall, 2022](#)). It integrates two established algorithms, SIMPLE and PISO, into a cohesive framework. During each iteration, the motion of the floating body is calculated first, followed by a mesh update, and the air-water interface is then captured using the VOF method. The PISO cycle specifically handles the coupling between pressure and velocity. To ensure seamless interaction with the mooring line solver, MoorDyn, the rigid body motion solver incorporates the restraints named 'MoorDynR'. These activate MoorDyn when force calculations are needed. This triggers a reciprocal exchange of information between the solvers, including data on position, pressure, velocity, acceleration at the nodes, forces and moments acting on the floating body, and tension in the mooring lines. Typically, two iterations of the PIMPLE cycle are sufficient to achieve convergence in the motion simulation. Finally, [Table 2](#) presents the key parameters employed in the numerical model to characterize the structure and mooring system. This overview facilitates the assessment of consistency between the numerical inputs and the experimental conditions.

2.3.1.3. Computational domain and boundary condition. In order to obtain a model that accurately simulates the dynamic behaviour of the FOWT analysed, it was decided to define a computational domain that reproduced both the geometry and the physics of the experimental phase. Being a multiphase simulation, the computational domain is divided into an upper domain which simulates the presence of air and a lower domain simulating the presence of water. The dimensions of the lower domain were defined to accurately replicate those of the experimental test basin. This approach, widely established in the literature, ensures a realistic representation of the physical phenomena observed under laboratory conditions ([Chen and Hall, 2022](#); [Wang et al., 2022](#); [Tran et al., 2024](#)). Accordingly, the domain is characterised by a length of 20 m along the x -axis and a width of 30 m along the y -axis. This configuration precisely replicates the presence of a central pit at a depth of 6 m, while the remaining sections are maintained at a depth of 3 m. The upper section of the calculation domain simulating the air phase was raised to a height of 4 m, i.e. 1.7 times the height of the hub (rounded up), providing a vertical clearance of 1 m above the highest point of the geometry, corresponding to the upper tip of

Table 2

Main parameters used in the numerical model to describe the structure and mooring system. This overview facilitates the assessment of consistency between the numerical inputs and the experimental data, which can be found in Table 1.

Properties	Units	Value
Center of Mass	m	(0; 0; -2.25)
Mass	kg	122.13
Roll inertia	$kg \cdot m^2$	41.3
Pitch inertia	$kg \cdot m^2$	41.3
Yaw inertia	$kg \cdot m^2$	1.6
EA	N	48.77
Ustretched mooring lenght	m	1.79
	m	(0.12; 0.00; -1.75)
Fairlead points	m	(-0.06; 0.10; -1.75)
	m	(-0.06; -0.10; -1.75)
	m	(2.05; 0.00; -3.00)
Anchor points	m	(-1.03; 1.78; -3.00)
	m	(-1.03; -1.78; -3.00)

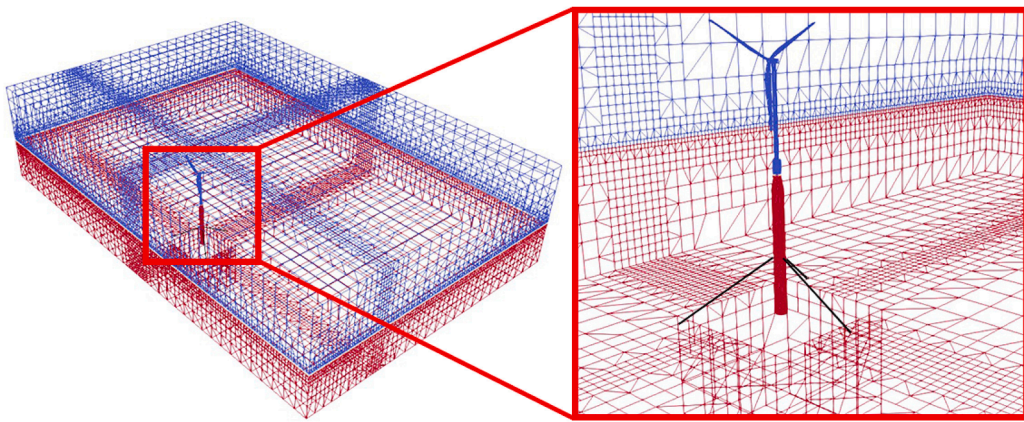


Fig. 4. Integrated representation of the numerical model. The computational domain is generated using blockMeshDict, ensuring an accurate representation of the basin dimensions, including the deep-water pit. The multiphase nature of the domain is defined through setFieldsDict, where the water phase is shown in red and the air phase in blue. The structure is incorporated within the domain using snappyHexMesh, while its motion is governed by dynamicMeshDict and dynamically coupled with the mooring system, modeled through MoorDyn.

the blades. Considering that aerodynamic loads are not taken into account and that this height is more than sufficient to guarantee the correct development of the wave, this size of the domain was considered an excellent compromise between the accuracy of the results and the reduction of the computational burden of the analysis. A brief sensitivity analysis on the domain height is presented in Appendix B, demonstrating that this assumption did not adversely affect the numerical results. Further increases in the upper boundary height produced virtually no change in the captured free-surface profile. To define the numerical wave tank, a background hexahedral mesh was first generated using the blockMesh utility. This initial step established a structured grid that served as the foundation for further refinement. In order to guarantee an accurate delineation of the pit and to differentiate between the sections corresponding to the two distinct phases, air and water, the entire domain was subdivided into a series of discrete blocks ensuring the correspondence between all nodes in the mesh. The computational domain was then enhanced and the target geometry integrated through the snappyHexMesh utility, which allowed for precise adaptation of the mesh to the geometry's features. Local refinement was controlled using refinement boxes, ensuring higher resolution in key areas while keeping the rest of the domain coarser to optimize computational efficiency. Specifically, three refinement boxes were aligned with the principal axes, serving multiple purposes. First, they enabled a more accurate representation of the geometry. Second, they facilitated the detailed capture of the free surface variation, crucial for accurately evaluating hydrodynamic loads. Finally, the refinement supported a precise numerical assessment of the structure's displacement field, ensuring reliability in the simulation results. Once the domain mesh was optimally defined, it was possible to achieve a good level of mesh accuracy, consisting of 291260 cells, without adding excessive computational burden. Fig. 4 shows the results of the mesh setting.

Boundary conditions specify how physical properties behave at the boundaries of the computational domain, ensuring the simulation accurately reflects the system's interactions with its surroundings. The upper boundary of the domain, designated as "atmosphere", defines the interface with the external atmospheric environment, serving as the boundary for atmospheric computations. The lower

Table 3

This Table summarizes the various boundary conditions applied to the computational domain, including the specifications for the fluid inlet and outlet, lateral boundaries, dynamic wall conditions for the structure. The boundary conditions are defined for the velocity field, pressure, μ_t , and turbulence model parameters k and ω (used in the $k - \omega$ SST model). Additionally, boundary conditions for the phase fraction field Alpha, representing the multiphase domain, are also provided.

Boundary	Velocity	Pressure	μ_t	k	ω	Alpha
Inlet	<i>waveVelocity</i>	<i>fixedFluxPressure</i>	<i>calculated</i>	<i>fixedValue</i>	<i>fixedValue</i>	<i>waveAlpha</i>
Outlet	<i>waveAbsorption2DVelocity</i>	<i>fixedFluxPressure</i>	<i>calculated</i>	<i>inletOutlet</i>	<i>inletOutlet</i>	<i>zeroGradient</i>
Atmosphere	<i>pressureInletOutletVelocity</i>	<i>totalPressure</i>	<i>calculated</i>	<i>inletOutlet</i>	<i>inletOutlet</i>	<i>inletOutlet</i>
Bottom	<i>noSlip</i>	<i>fixedFluxPressure</i>	<i>nutkWallFunction</i>	<i>kqRWallFunction</i>	<i>omegaWallFunction</i>	<i>zeroGradient</i>
Stationary Walls	<i>noSlip</i>	<i>fixedFluxPressure</i>	<i>nutkWallFunction</i>	<i>kqRWallFunction</i>	<i>omegaWallFunction</i>	<i>zeroGradient</i>
FOWT	<i>movingWallVelocity</i>	<i>fixedFluxPressure</i>	<i>nutkWallFunction</i>	<i>kqRWallFunction</i>	<i>omegaWallFunction</i>	<i>zeroGradient</i>

boundary, called "bottom", represents the basin floor and the base of the pit. The lateral boundaries are identified as "stationary walls", which model the side boundaries of the basin and the four walls of the pit. Additionally, the front boundary is configured as a wave inlet to enable wave generation, while the rear boundary includes wave absorbers designed to dissipate wave energy efficiently. To accurately configure the numerical model, it is essential to define the boundary conditions for pressure, velocity, wave characteristics, eddy viscosity μ_t , and the turbulence parameters k and ω . These conditions ensure the proper closure of the RANS equations and enable the simulation of the turbulent behavior of the two-phase system. Table 3 outlines the specific boundary conditions applied in the model discussed in this paper, providing a detailed overview of how each parameter was set for the simulation.

2.3.2. OpenFAST numerical model

The FOWT was also simulated using OpenFAST, an open-source framework developed by NREL for coupled time-domain analysis. In the present work, this tool allows the simultaneous consideration of structural and hydrodynamic aspects, providing a detailed and integrated representation of FOWT behavior under different loading conditions.

Structural dynamics of the structure was modeled via the ElastoDyn module. This module enables users to define initial conditions, mass properties, inertia properties and distributed parameters of the structure. It calculates the positions, velocities, and accelerations of critical points within the structure, representing the platform as a six-degree-of-freedom rigid body. The hydrodynamic response of the spar was captured using the SeaState and HydroDyn modules. SeaState generates three-dimensional time series for wave elevation, fluid velocity, and dynamic pressure across a computational grid refined near the free surface. HydroDyn interpolates these values at the nodes of the structure to compute wave-induced forces, fluid-inertia contributions, and viscous drag, while redistributing nodal loads to prevent discontinuities as the structure interacts with the free surface. Hydrostatic forces incorporate local surface slopes to enhance accuracy. For the spar-type floating structure studied, which is slender relative to the incident wavelength, hydrodynamic forces were evaluated using a strip-theory approach in combination with the relative form of Morison's equation. The spar geometry is represented using joints and straight circular members, with forces applied at the nodal points. Mooring dynamics were simulated using MAP++, which applies a quasi-static approach to determine equilibrium configurations under environmental forcing. Each mooring line is divided into segments characterized by nonlinear stiffness, which allows for the accurate representation of the primary geometric and material nonlinearities. This formulation enables a faithful representation of the three-dimensional response of the mooring system and is fully integrated with OpenFAST for coupled simulations.

Additional technical details on OpenFAST's treatment of hydrodynamic forces, structural response, and mooring line behavior are available in the official documentation (National Renewable Energy Laboratory (NREL), 2023; Masciola, 2025).

3. Results and discussion

This section outlines the results of the present study. In particular, Section 3.1 illustrates the results of the validation of the proposed analytical model. This validation was performed by comparing the analytical results with the data derived from the experimental campaign previously described (Section 2.2). Instead, Section 3.2 reports the results related to the analysis and evaluation of the performance of the proposed analytical model, conducted by comparing the analytical results with the outcomes of the previously described numerical models (Section 2.3). Finally, Section 3.3 provides a detailed discussion on the validity limits of the analytical model and its fields of applicability.

It is worth noting that the proposed formulation is fully analytical and does not rely on geometric modeling, numerical methods, or discretization processes. In this manuscript, in order to automate the calculation for different time instants, the analytical model presented was implemented in Matlab R2022a. This tool enabled the calculation and visualisation of results for our specific case of study and allowed us an easier comparison with experimental and numerical data. Fig. 5 clearly outlines the required inputs and the sequential steps necessary to apply the proposed analytical method, explicitly utilizing the equations introduced in Section 2.1 and Appendix A.

The analytical and numerical models were developed using input data directly obtained from the experimental campaign, with no adjustments or variations applied. This approach guarantees that all analysis are based on identical parameter values, ensuring consistency and accuracy in the comparison of results. A summary of the input parameters adopted in the analytical model is provided in Table 4, which can be directly compared with the key data of the experimental setup (Table 1). A necessary clarification concerns the selected value of c_x . In line with the assumptions outlined in Section 2.1, the value provided in the Table 4 was used consistently

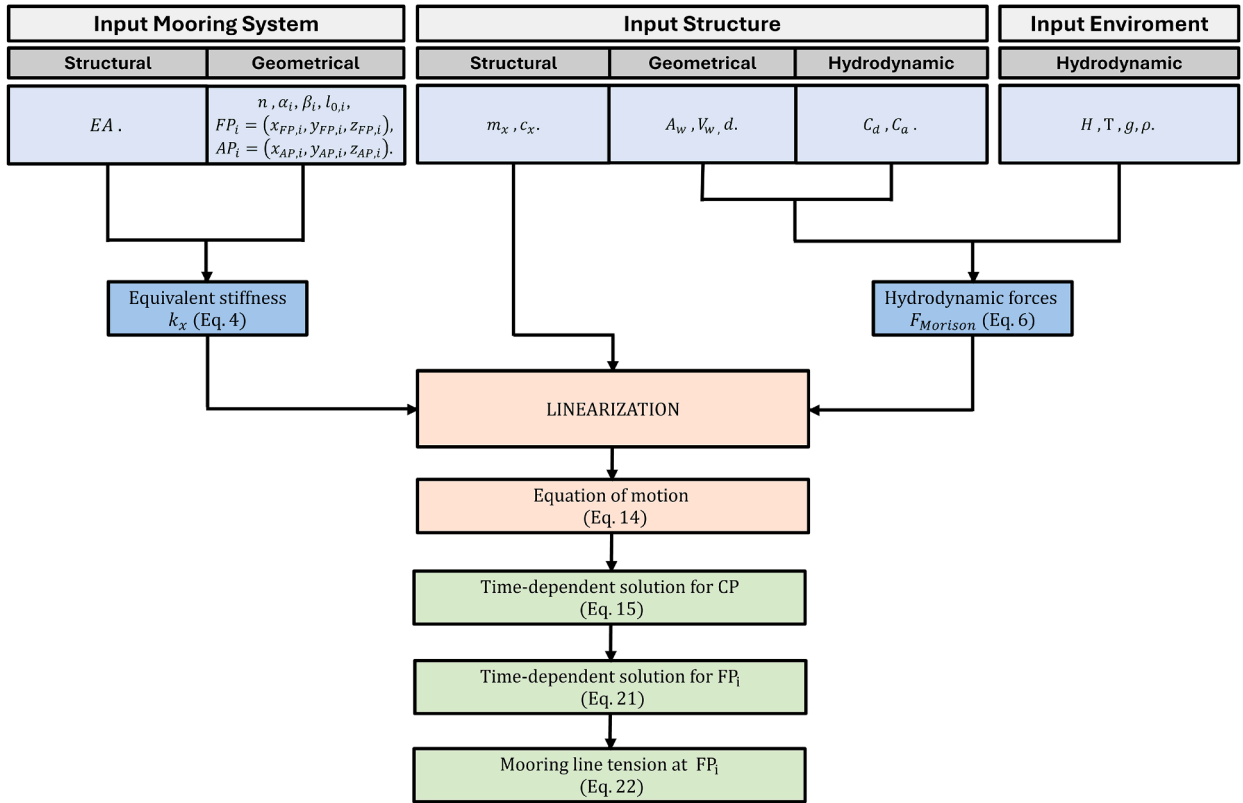


Fig. 5. This figure presents the various inputs required for the application of the proposed analytical method, referring to the structure, mooring system, and wave conditions. Specifically, it details how these inputs contribute to the calculation of different components by applying the equations introduced in Section 2.1 and Appendix A. Consequently, it is possible to solve the time-dependent solution at any given instant to first obtain the structural displacements and subsequently the tensions in the mooring lines at the fairlead points.

across all analysis to guarantee a structural damping ratio of 1% with respect to critical damping c_{cr} , compatibly with the typical values adopted for the structure under investigation (Jonkman, 2010). In the absence of specific data, the values that can be assumed for the structural damping ratio, according to the various industry standards and guidelines, typically range between 1% and 5%, depending on the loads being considered and the analysis being performed (van Vondelen et al., 2022). Finally, the values used for C_d and C_a are those recommended for the spar type OC3-Hywind floating substructure, as indicated in Jonkman (2010).

3.1. Analytical model validation

This section presents the results obtained from the proposed analytical model, comparing them with experimental data. Initially, the time-domain results are compared, focusing on the FSE to validate the correct modeling of the wave motion. Subsequently, the accuracy of the proposed linearization method for the force system is evaluated, assessing its reliability (Section 3.1.1). The results are then analyzed in the frequency domain in terms of displacements to verify the model’s ability to capture the natural frequency of the system and the forcing frequency, as well as to assess the dynamic response of the structure (Section 3.1.2). A convergence analysis of the analytical results with respect to the experimental data was performed, followed by a comparison of displacement results and mooring line tensions in the time domain (Section 3.1.3). To evaluate and validate the proposed model, a set of six distinct tests was selected from those conducted during the experimental campaign. Specifically, six tests were chosen in which the experimental model was subjected to regular wave conditions. The selected tests are summarized in the Table 5. The wave set was carefully selected to include variations not only in wave height and period, but also in wavelength, wave steepness, and nonlinearity, in order to cover a wide range of conditions and ensure a thorough assessment of the model’s applicability.

In this study, regular wave conditions were selected to provide a clear and controlled framework for the validation of the proposed analytical model. Regular waves enable a direct interpretation of the system’s response and are particularly suitable for the validation of analytical formulations. Although the analysis of the structure’s response under irregular wave conditions is essential for a complete evaluation of system performance, the controlled nature of regular wave tests makes them particularly effective for parametric analysis to identify key system parameters such as stiffness, mass, pretension and mooring configuration. Conducting these analysis under regular wave conditions represents a necessary and preliminary step in the design process, as it enables a systematic investigation of the system’s fundamental dynamic characteristics. This approach ensures a robust basis for subsequent evaluations under irregular

Table 4

Input parameters for the structure and mooring system used in the analytical model. The values were directly derived from the experimental campaign and can be cross-checked with the experimental data reported in Table 1.

Input Mooring System			Input Structure		
Parameter	Units	Value	Parameter	Units	Value
EA	N	48.77			
n	–	3	m_x	kg	122.13
		0			
α_i	deg	60	c_x	Ns/m	2.13
		60			
		32.6	A_w	m^2	0.69
β_i	deg	32.6			
	–	32.6	V_w	m^3	0.12
$l_{0,i}$	m	1.79			
		(0.12; 0.00; –1.75)	d	m	3
FP_i	m	(–0.06; 0.10; –1.75)			
		(–0.06; –0.10; –1.75)	C_d	–	0.6
		(2.05; 0.00; –3.00)			
AP_i	m	(–1.03; 1.78; –3.00)	C_a	–	0.97
		(–1.03; –1.78; –3.00)			

Table 5

Test matrix selected for the validation of the analytical model to cover a range of heights, periods, wavelengths, steepness values, and nonlinearity levels, in order to provide a comprehensive set of test cases for model validation.

Test Number	Waves	H	T	Direction	λ	$\frac{H}{\lambda}$	$\kappa \frac{H}{2}$
	–	[m]	[s]	[deg]	[m]	[–]	[–]
1	Regular	0.05	1.6	0	3.996	0.013	0.039
2	Regular	0.05	1.9	0	5.623	0.009	0.028
3	Regular	0.13	1.6	0	3.996	0.033	0.102
4	Regular	0.13	2.2	0	7.461	0.017	0.055
5	Regular	0.25	1.6	0	3.996	0.063	0.196
6	Regular	0.25	1.9	0	5.623	0.044	0.140

wave conditions and for the verification of system performance at the limit states.

For clarity, hereafter the different tests will be referred to as T followed by the corresponding test number (e.g., T1, T2, etc.)

3.1.1. FSE and force linearisation validation

In this section, the results in the time domain of the FSE and the acting forces are analyzed. Accurately capturing the variation of the free surface is crucial, as it is closely related to the system of hydrodynamic forces acting on the structure. These forces drive the displacements of the structure, which, in turn, influence the variations in tension within the mooring lines. Fig. 6 presents a comparison between the FSE calculated with the analytical model and those obtained from experimental data.

For the different tests analyzed, a high degree of agreement is observed between the results from the methods mentioned. In T1 and T2, Fig. 6(a) and (c), there is a significant match both in terms of period and amplitude, as well as in the temporal development. Regarding T3, T4, T5 and T6, respectively Fig. 6(e), (g), (i) and (k), an excellent agreement is observed in terms of period and wave height, accompanied by a slight temporal phase shift of the order of 10^{-1} s. This phase shift can be attributed to the initial time required by the wave generators in the experimental tests to start operating and reach the desired wave height. In the analytical model, this effect could have been taken into account through a ramp-time function, but was not implemented, as it is a feature specific to the experimental tests and not physically relevant in the real context. Once the reliability of the analytical model in evaluating wave motion and, consequently, the hydrodynamic forces was verified, the acting forces for each of the six tests analyzed are presented in Fig. 6(b), (d), (f), (h), (j) and (l). Specifically, the forces calculated using the well-known Morison equation are compared with those obtained through the linearization approach proposed in this analytical model and explained in Section 2.1.2. The comparison shows a perfect agreement between the two loading histories, confirming the validity of the adopted linearization method. It is also observed that the Fourier series expansion in the case under investigation considered the first 5 harmonics.

3.1.2. Frequency-domain results

In the present section, the displacement results in the frequency domain are analyzed to assess the ability of the analytical model to accurately capture the dynamic characteristics of the analyzed structure. As highlighted in Section 2.1, the equation of motion consists of two main components: the transient contribution, related to the natural frequency of the structure, and the stationary contribution, primarily dominated by the forcing function. The transient phase is characterized by a decay period, after which its effects become

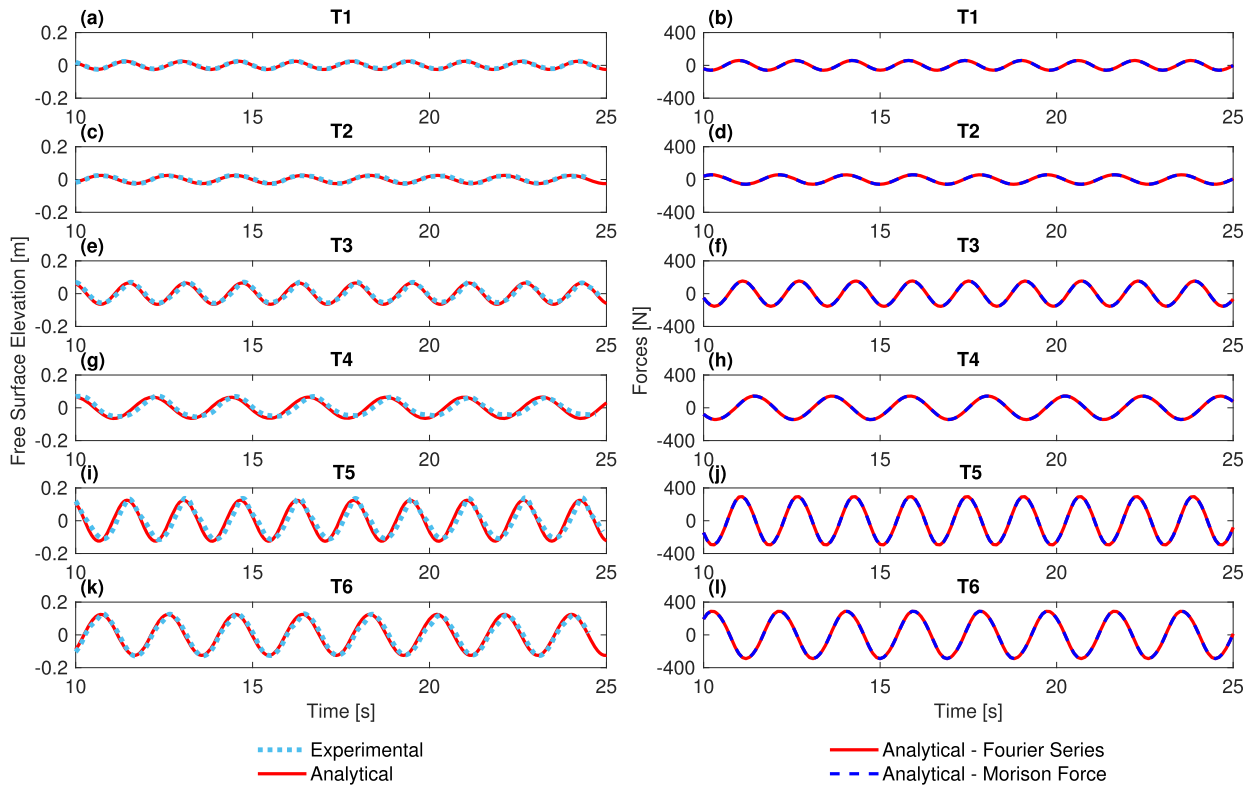


Fig. 6. Left: time-domain comparison of analytical and experimental free surface elevation results for Test 1 (a), Test 2 (c), Test 3 (e), Test 4 (g), Test 5 (i), and Test 6 (k). Right: time-domain comparison of forces computed using Morison’s equation and the linearization method proposed in this study for Test 1 (b), Test 2 (d), Test 3 (f), Test 4 (h), Test 5 (j), and Test 6 (l).

negligible, allowing the stationary phase to prevail. In the experimental tests, the transient phase is not visible for several reasons. During tank tests with regular waves, data collection typically begins only after the system has reached a steady-state condition, to avoid interference from the initial acceleration or the adjustment of regular waves. Additionally, the waves in the tank are generated in a controlled, continuous manner, without any impulses or sudden variations that could trigger a significant transient phase. In contrast, in the analytical model, the force is assumed to be applied instantaneously to the structure, generating a marked transient component that is not observed in the experimental results. However, the analytical modeling of the transient phase is crucial, as demonstrated by the analysis of displacement results in the frequency domain, shown in Fig. 7. The results for T3, Fig. 7(a), T4, Fig. 7(b), and T6, Fig. 7(c), were analyzed using Fast Fourier Transformation (FFT) of the time-domain results. The results for the other tests are not shown, as they were conducted on the same structure and with the same wave period as the tests already presented, and would therefore exhibit identical frequency content. The main objective of this analysis is to verify the analytical model’s ability to identify the dominant frequencies in terms of both acting forces and structural response. It can be seen that, thanks to the analytical modeling of the transient phase, it is possible to capture not only the wave frequency but also the structural response frequency. It can be observed that, for all tests, the analytical model effectively captures the system’s surge frequency, which is approximately 0.075 Hz, as well as the respective frequencies of the acting forces, 0.625 Hz for T3 (Fig. 7(a)), 0.449 Hz for T4 (Fig. 7(b)) and 0.525 Hz for T6 (Fig. 7(c)). A detailed analysis of the entire Fig. 7 highlights that, while the dominant frequencies are accurately captured, a moderate amplitude discrepancy is observed between the analytical model and the experimental data. The observed amplitude discrepancy is primarily attributed to the higher energy content in the dynamic response predicted by the analytical model, which results precisely from the inclusion of transient phase in the formulation. These transient effects, as previously discussed, are absent in the experimental measurements, since data acquisition during the tank tests was initiated only after the system had reached a steady-state condition. Nevertheless, this difference confirms that our analytical model provides conservative predictions, which is a desirable feature at the preliminary design stage, ensuring safe estimations of the dynamic response.

3.1.3. Convergence analysis and time-domain results

This section presents the results of the convergence analysis of the analytical model in comparison with the experimental data. Subsequently, the time-domain results for displacements and tensions will be presented. Convergence analysis were performed on the results obtained from the analytical model, as shown in Fig. 8, for each test. Convergence analysis were conducted by assessing the absolute error, at each time step, between the analytical model results and the experimental data in terms of displacement. The objective was to identify the point in time at which the analytical model results can be considered sufficiently reliable. The analysis

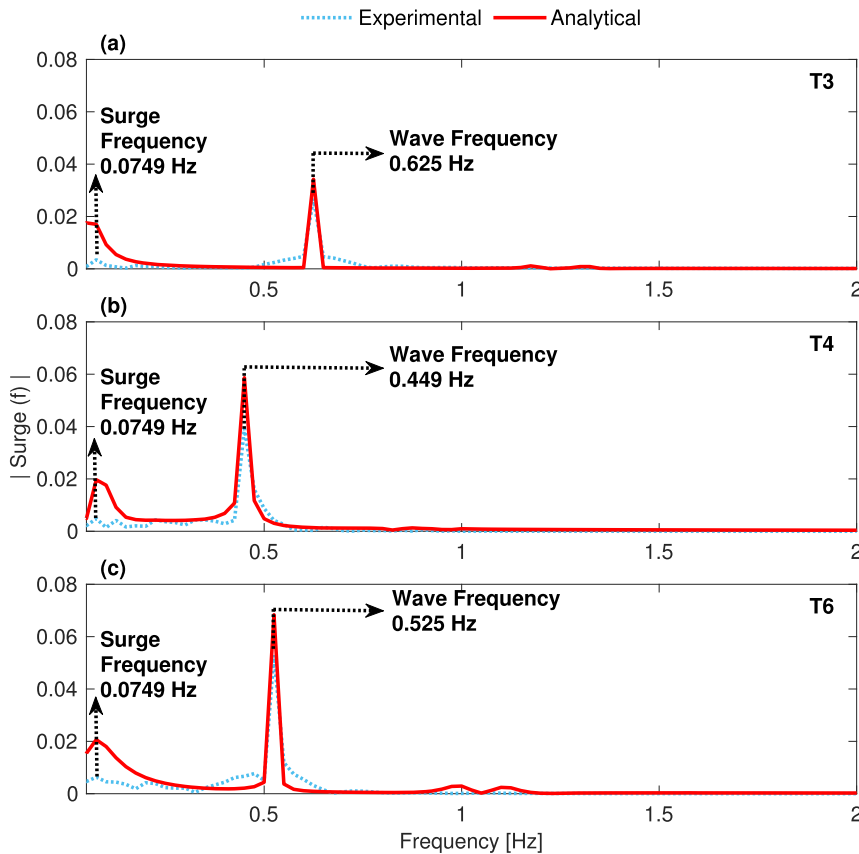


Fig. 7. Frequency-domain comparison of experimental and analytical results for surge displacement, obtained using Fast Fourier Transform (FFT) for Test 3 (a), Test 4 (b) and Test 6 (c). The analysis highlights the identification of both surge and wave frequencies, demonstrating a high level of accuracy between the experimental data and the results derived from the proposed analytical method.

reveal that, in the initial seconds, there are discrepancies when compared to the experimental results, which can be attributed to the transient phase predicted by the analytical model. Since this phase is not observable in the experimental tests for the reasons mentioned in Section 3.2, the subsequent results will be presented focusing on the stationary phase, which represents the state of greatest interest for the analysis.

The results concerning the surge displacements of the structure and the tensions in the mooring lines, calculated using the analytical model and compared with experimental data, are analyzed. In particular, Fig. 9 shows the results in terms of surge displacement for the different tests performed, while Fig. 10 shows the results in terms of mooring tension. For T1 and T2, the analytical model shows overall good agreement with the displacements (Fig. 9(a) and (b)), which are slightly overestimated, while the tensions (Fig. 10(a) and (b)) are calculated with high accuracy. In the cases of T3, T5, and T6, an excellent agreement with the experimental results is achieved. As shown in Fig. 9(c), (e), and (f), the analytical model demonstrates a very high level of accuracy in capturing the surge displacements. A similarly strong agreement is observed in the evaluation of mooring line tensions, as illustrated in Fig. 10(c), (e), and (f). With regard to T4 the analytical results show good agreement with the experimental data, demonstrating a significant correspondence in terms of the overall trend, with a slight overestimation of results. It is worth noting that the agreement with mooring tensions results is more pronounced (Fig. 10(d)) than that observed for displacements (Fig. 9(d)). The small discrepancies observed may be attributed to nonlinear phenomena affecting the dynamic behavior, which are not included in the analytical model, or to potential variations during the experimental data acquisition that could have influenced the signal peaks.

3.2. Performance analysis and evaluation

In this section, an analysis and evaluation of performance of the proposed analytical formulation are presented. The analytical model introduced in Section 2.1 is based on specific assumptions, including the decoupling of DoF, reduction to a single DoF, and linearization of the problem. The primary objective of this study is to quantify the reduction in accuracy introduced by the adopted assumptions when compared to more sophisticated modeling approaches, and subsequently to evaluate the potential benefits and limitations of utilizing a simplified methodology during the early design stages. To achieve this, two fully coupled, nonlinear, three-dimensional numerical models were developed in OpenFOAM and OpenFAST, as described in Section 2.3. The results obtained from

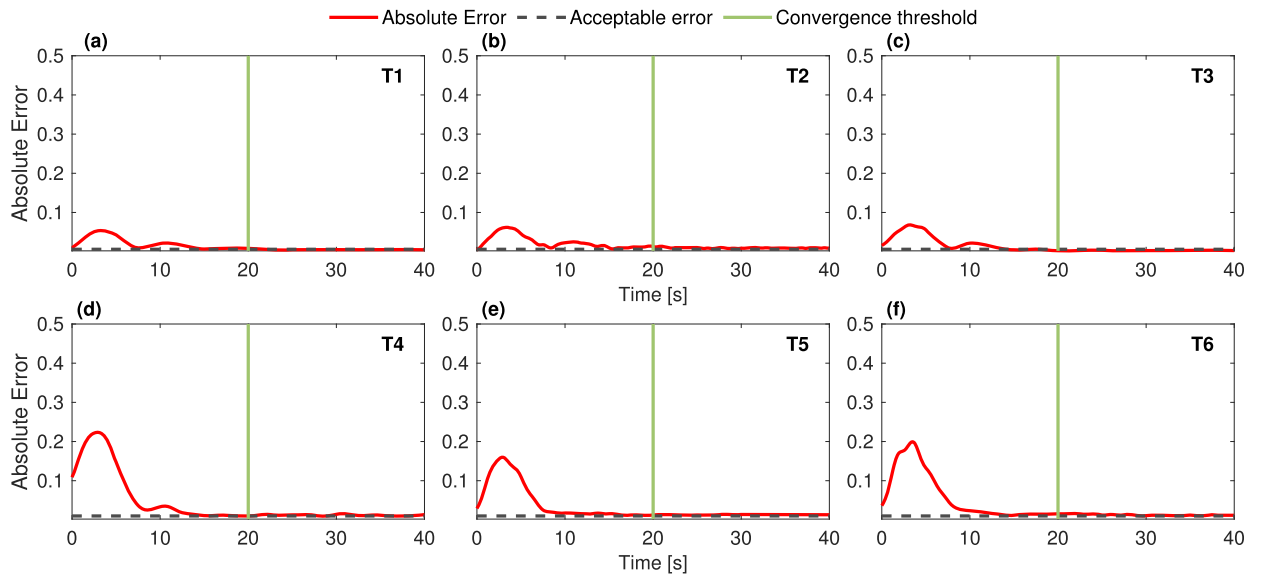


Fig. 8. Convergence analysis of the analytical model for Test 1 (a), Test 2 (b), Test 3 (c), Test 4 (d), Test 5 (e) and Test 6 (f), focusing on the displacements calculated from the equation of motion formulated in this study. The analysis quantifies the absolute error between the analytical predictions and the experimental data, providing an assessment of the model’s ability to accurately capture the dynamic response. Convergence is achieved at the completion of the transient phase of the motion, ensuring the reliability of the numerical results.

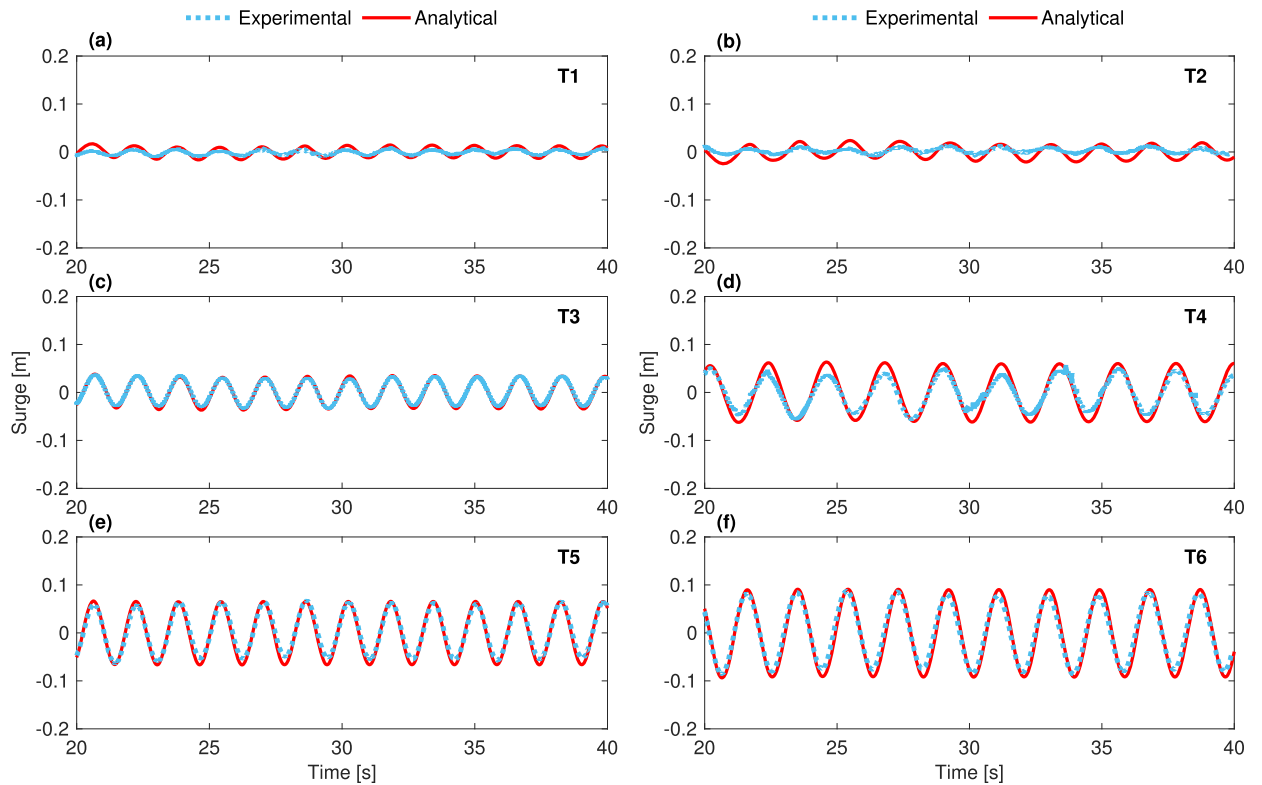


Fig. 9. Time-domain comparison of surge displacements obtained from the analytical model and experimental data, considering an initial time of 20s. This time instant marks the onset of convergence between the analytical and experimental results, as indicated in Fig. 8. The analysis is presented for the entire test set: Test 1 (a), Test 2 (b), Test 3 (c), Test 4 (d), Test 5 (e) and Test 6 (f).

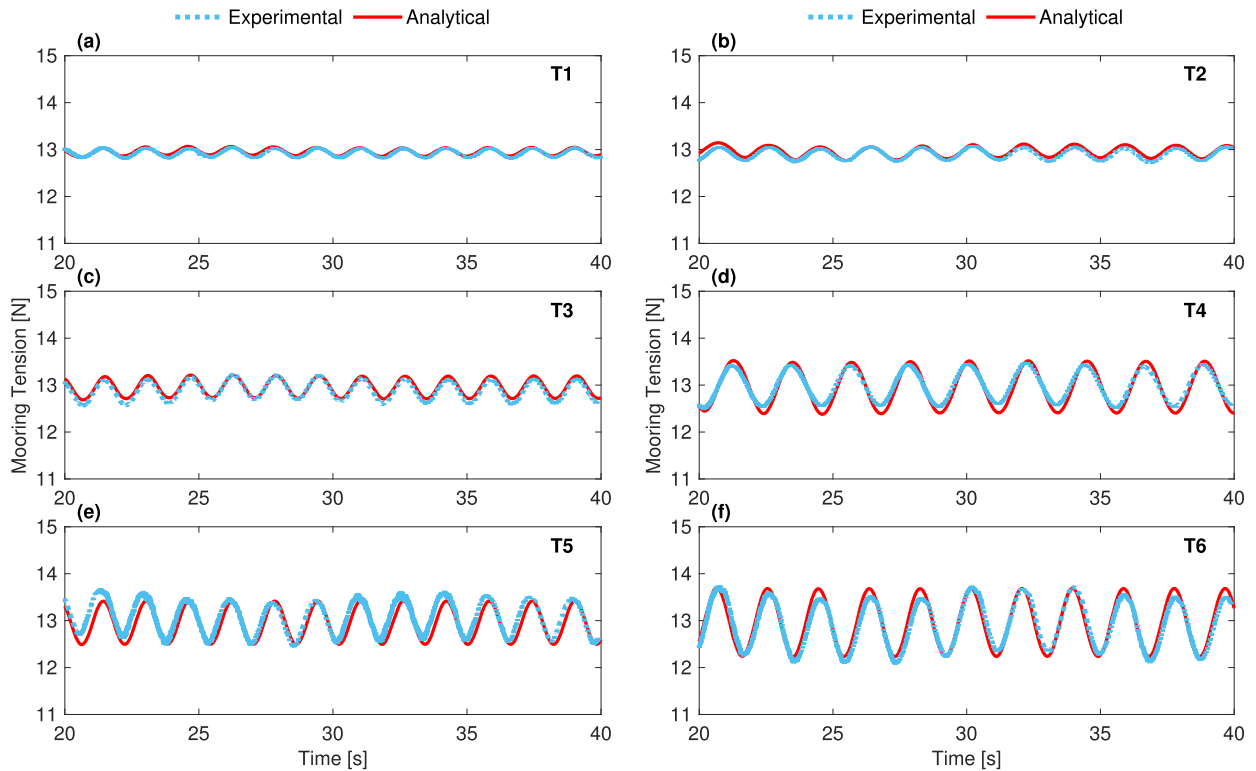


Fig. 10. Time-domain comparison of mooring tension obtained from the analytical model, experimental data, considering an initial time of 20s. This time instant marks the onset of convergence between the analytical and experimental results, as indicated in Fig. 8. The analysis is presented for the entire test set: Test 1 (a), Test 2 (b), Test 3 (c), Test 4 (d), Test 5 (e) and Test 6 (f).

the analytical formulation were compared with those from the numerical simulations. The numerical simulations were specifically designed to enable a direct comparison with the analytical results, maintaining consistent boundary conditions between the approaches, particularly with regard to wave representation. Indeed, although it is recognized that the adoption of regular waves modeled according to Stokes' third-order wave theory could have further enhanced the numerical accuracy and reduced discrepancies with experimental data, this refinement was intentionally not pursued in OpenFOAM to ensure consistency with the wave formulation adopted in the analytical model and in the OpenFAST numerical model (Stokes I).

For this phase, three representative tests were selected from the overall test set: T1, T3, and T4. The selected tests were chosen as representative of the overall validation outcomes: T3 demonstrated excellent agreement with experimental results in terms of both displacement and mooring tension; T1 showed a slight overestimation of displacements while maintaining excellent agreement for mooring tensions; T4 exhibited a slight overestimation in both displacements and tensions. The comparison was first carried out in the time domain by analyzing FSE, surge displacement, and mooring tension, comparing the analytical results, numerical simulations, and experimental data. Subsequently, the same results were analyzed in terms of key parameters relevant to the preliminary design phases of FOWTs. Finally, performance assessments of the proposed analytical model were conducted.

Fig. 11 presents a comparison between analytical and numerical results in the time domain in terms of FSE, referenced against the experimental data. It can be observed that both analytical and numerical results exhibit comparable levels of reliability when validated against the experimental measurements. In particular, the results obtained from OpenFAST are, in all cases, in very close agreement with those derived from the analytical model, both in terms of wave height and period, as well as in their temporal evolution. This close correspondence primarily arises from the use of the same wave formulation, without the inclusion of nonlinear effects, unlike the OpenFOAM model, in which turbulent phenomena are explicitly considered. For cases T1 and T4, the numerical OpenFOAM results show a good agreement in terms of wave height and period, although a slight temporal phase shift is noticeable. As discussed in Section 3.1.1, this phase shift can be attributed to the initial time required for the wave generators in the experimental setup to activate and reach the target wave height. In the OpenFOAM numerical model, this aspect was partially addressed by implementing a ramp-time function, which allows the wave height to gradually reach the desired value. However, this approach does not explicitly model the start-up time of the physical wave generators, thereby explaining the persistence of a minor phase lag. In contrast, for case T3, the OpenFOAM numerical results exhibit an almost perfect agreement with the experimental time history. Nonetheless, a slight underestimation of the wave amplitude is observed in the numerical solution. This discrepancy could be related to the turbulent kinetic energy (k) and dissipation rate (ω) parameters adopted in the turbulence model. This highlights the inherent uncertainties associated with the calibration of turbulence model parameters, which is a known limitation of the numerical methodology. Such

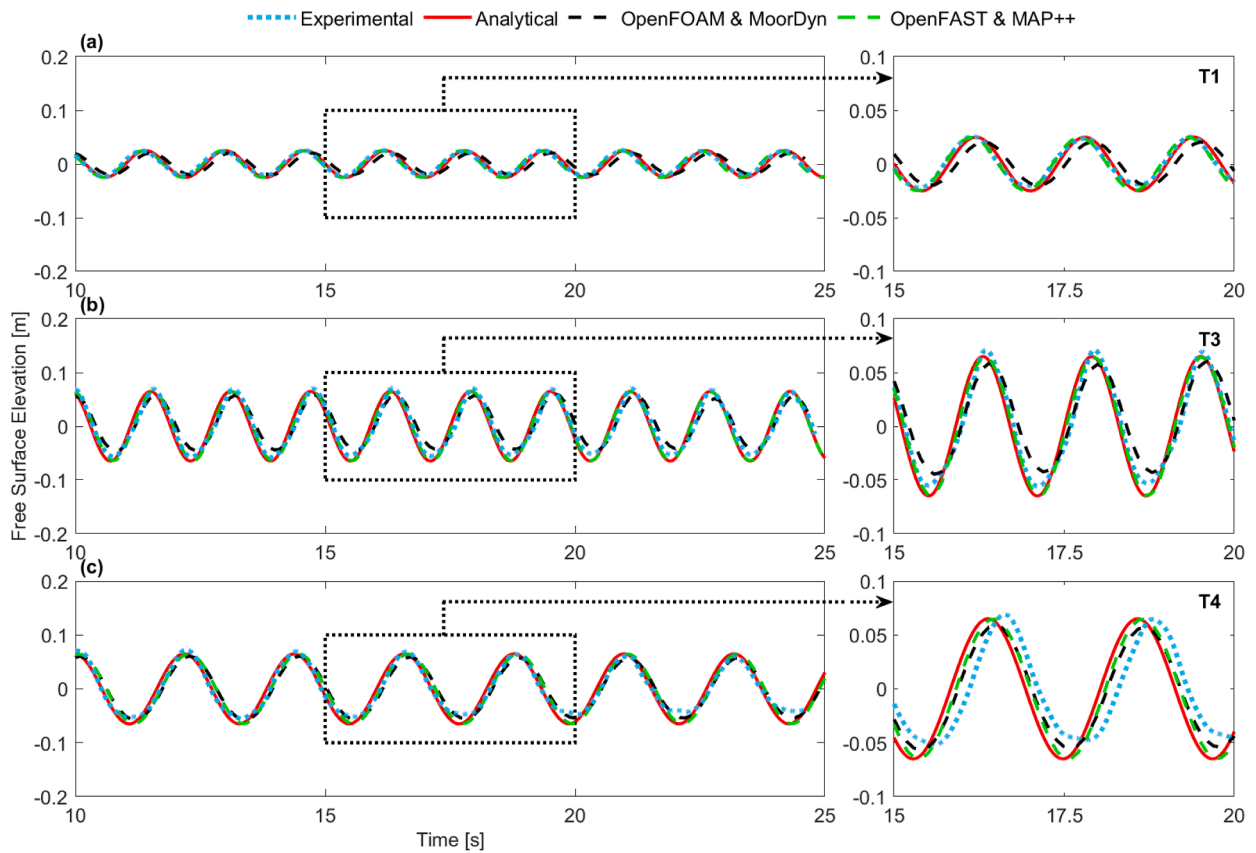


Fig. 11. Comparison of the time domain accuracy of analytical and numerical results against experimental free surface elevation data for Test 1 (a), Test 3 (b), Test 4 (c).

uncertainties pose additional challenges when applying these methods in the early design stages, where, both in real-world scenarios and in designing experimental campaigns, reference data for the calibration of turbulence parameters is typically unavailable. Moreover, enhancing the reliability of the model would require significantly higher computational resources, which may not always be feasible at this stage.

Figs. 12 and 13 present the time-domain results in terms of surge displacement and mooring line tension, comparing both analytical and numerical predictions against the experimental data. Across the different test cases analyzed (T1, T3, and T4), the accuracy of the analytical results is found to be highly comparable to that of the numerical simulations, although the two numerical models exhibit some differences in their results. In particular, OpenFAST provides fairly accurate predictions in terms of both amplitude and oscillation period of displacements and tensions across the various test cases, confirming the trends highlighted by the analytical model, except for T4. In this case, OpenFAST shows a closer agreement with the experimental data in terms of overall behavior, although it slightly underestimates the peak values. The agreement with OpenFOAM, on the other hand, occurs not only in terms of displacement amplitude and oscillation period but also in terms of the accuracy trends observed across the different tests. Specifically, consistent with the analytical results, the numerical outcomes for T1 slightly overestimate surge displacements while providing a more accurate prediction of mooring line tensions. For T3, the numerical results demonstrate a high level of accuracy for both surge displacements and mooring tensions. For T4, the OpenFOAM numerical results show a slight overestimation of both displacements and tensions relative to the experimental data, with a more pronounced deviation than that observed in the analytical results. These are particularly significant findings, as they raise some important considerations. First and foremost, an intrinsic challenge in numerical modelling is the need to set and calibrate a large number of parameters that influence the simulation outputs and are often difficult to validate in the early design stages, as the structure being developed typically lacks experimental or field data. Consequently, such parameters must often be assumed by analogy with other projects or estimated empirically, introducing a certain degree of uncertainty into the modelling process. Moreover, as discussed in Section 3.1.1, these discrepancies with the experimental data can be associated with nonlinear effects. However, the complexity of such phenomena makes them difficult to control. Although nonlinearities are accounted for in the numerical model, achieving higher levels of accuracy through numerical simulations is not guaranteed, as the exact sources and contributions of these nonlinear effects are often challenging to identify. The number of parameters and boundary conditions that would need to be adjusted and calibrated within such a numerical model to improve the representation of nonlinearities is considerable. This leads to a level of complexity that is difficult to manage during the early design stages. As

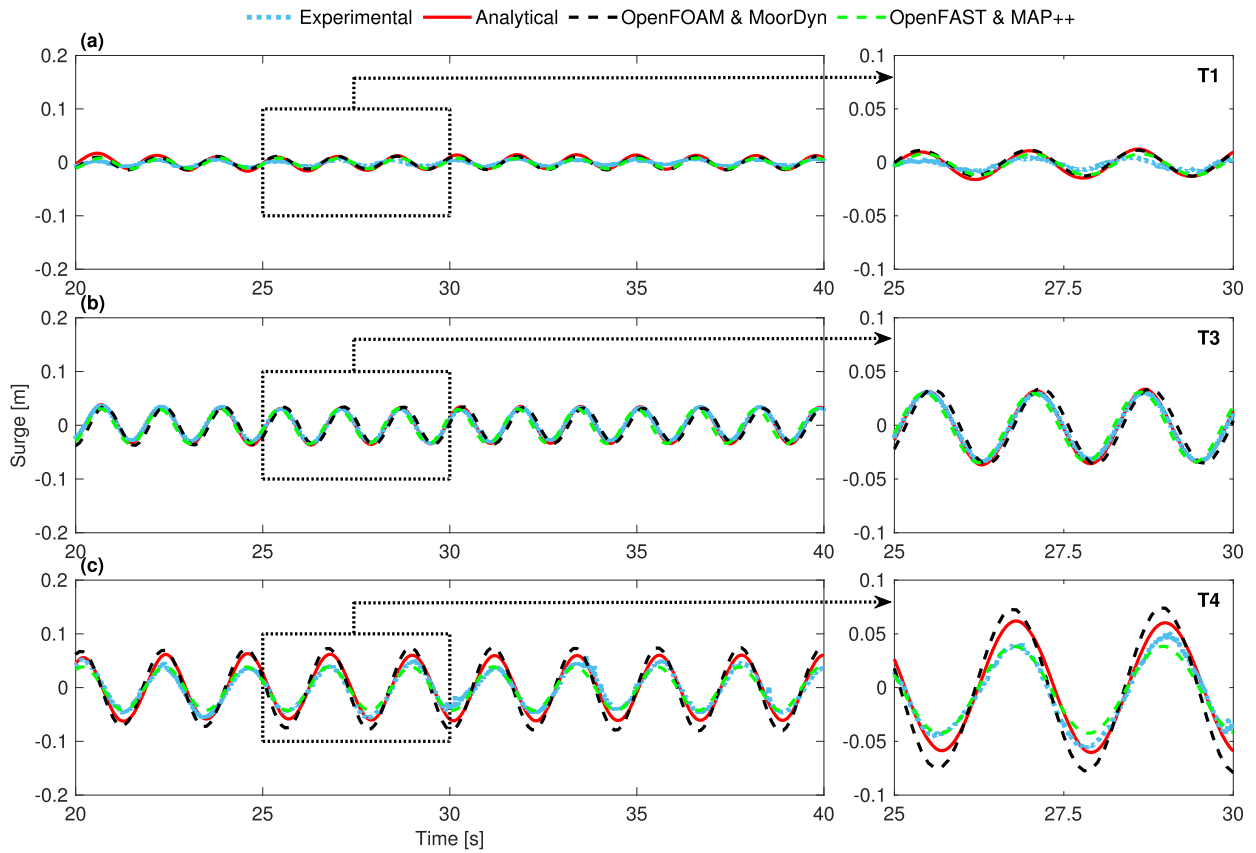


Fig. 12. Comparison of the time domain accuracy of analytical and numerical results against experimental surge displacements data for Test 1 (a), Test 3 (b), Test 4 (c).

previously discussed for FSE, proper model tuning would require sensitivity analysis and extensive parametric studies, which in turn demand a large number of simulations. In some cases, it may also be necessary to refine the mesh by increasing the grid density or to employ more advanced solution algorithms, which would inevitably lead to a significant increase in computational cost. Even in scenarios where computational resources are not a limiting factor, and assuming that the correct set of parameters and boundary conditions could be identified to achieve higher accuracy, the substantial increase in simulation time during the preliminary design phase would, in most practical applications, remain unsustainable.

In light of these considerations, attention is now directed towards key parameters relevant to the preliminary design stages of FOWTs, and a performance analysis is subsequently conducted. Fig. 14 presents the maximum positive (a) and negative (b) displacement values of the structure, the maximum (c) and minimum (d) tension values in the mooring lines as well as the pretension value (e), obtained from the analytical model and compared with experimental data and numerical results for the three tests analyzed. The evaluation of the key parameters was carried out over the entire time window illustrated in Figs. 12 and 13, in compliance with the convergence analysis, except for the pretension, which, by definition, was determined at the initial time in the absence of any external loads. As previously observed in the time domain, a good agreement is evident between the analytical results and the experimental data, which is further confirmed by the predictions from both numerical models.

Fig. 15 correlates displacements with the predictions for the values already defined in Fig. 14.

It can be visually observed that there is an approximately linear relationship between the displacement and tension results, which is confirmed by both the analytical and numerical outcomes. The Pearson Correlation Coefficient is a statistical measure that quantifies the strength and direction of a linear relationship between two numerical variables. It is calculated as the ratio of the covariance of the two variables to the product of their standard deviations. The coefficient ranges from -1 to 1 , where the extreme values indicate a perfect negative or positive linear relationship, while a value of 0 suggests no linear correlation. The Pearson coefficients calculated for the experimental data, as well as for the analytical and numerical results, are shown in the Table 6. The results demonstrate a significant linear relationship, with a value of $r = 0.989$ for the experimental data, confirming that this relationship is captured with high accuracy by the analytical and numerical models, which yield errors of 0.4% for the analytical model, and 0.4% and 0.6% for the OpenFOAM and OpenFAST numerical models, respectively.

To quantitatively assess the accuracy and performance of the model in terms of maximum and minimum displacements and tensions, several metrics were considered: the Mean Absolute Error (MAE), which represents the average of the absolute errors

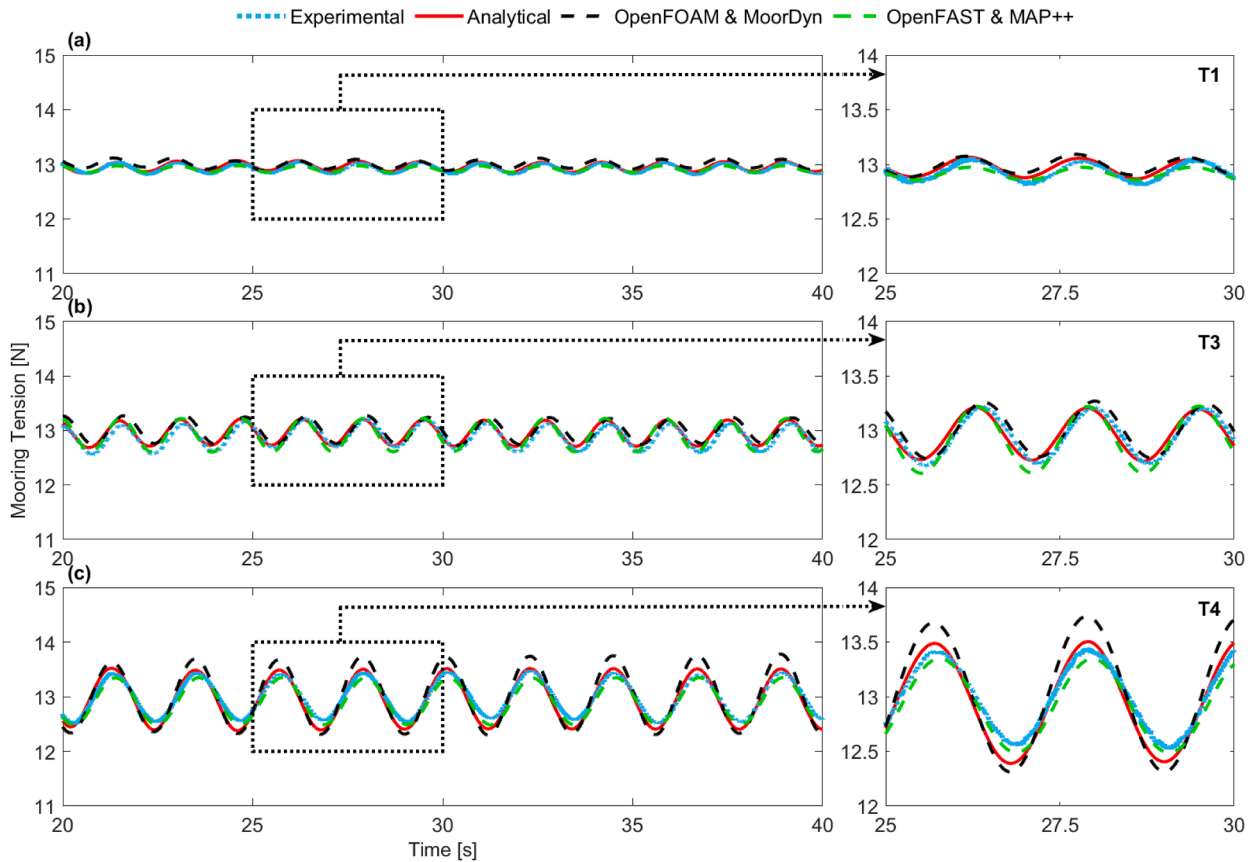


Fig. 13. Comparison of the time domain accuracy of analytical and numerical results against experimental mooring tension data for Test 1 (a), Test 3 (b), Test 4 (c).

Table 6

Comparison of the Pearson Correlation Coefficients for the tension-displacement relationship, derived from experimental, analytical, and numerical results. These coefficients are obtained based on the data presented in Fig. 14, providing a quantitative measure of the linear correlation between displacement and tension across the different test conditions.

Surge-Tension	Experimental	Analytical	OpenFOAM & MoorDyn	OpenFAST & MAP++
r	0.989	0.993	0.993	0.995

between the observed experimental values and the calculated ones; the Mean Absolute Percentage Error (MAPE), which quantifies the average absolute error as a percentage of the predicted values compared to the observed ones; the Root Mean Square Error (RMSE), which measures the mean squared error; and finally, the R^2 coefficient, also known as the Coefficient of Determination, which evaluates how well a predictive model fits the observed data (with a value of 1 indicating perfect explanation of the variance and 0 indicating no explanatory power). It is found that the analytical model yields a very low MAPE, indicating a high level of accuracy, which translates into a MAPE generally below 1%. The RMSE values are close to 0, while the R^2 values are near unity, confirming the reliability of the results obtained using this analytical model. The results are shown in Table 7 and compared with those from the numerical model, highlighting the achievement of good levels of accuracy in the predictions.

The results presented in this section demonstrate the analytical model’s ability to accurately compute the natural surge frequency of the structure, efficiently assess the damping effects, satisfactorily capture the dynamic response in terms of displacements, and sufficiently accurately estimate the dynamic behavior of the tensions in the mooring lines. These results highlight not only the capability of the proposed analytical model to describe the physical phenomenon from a global dynamic perspective but also its ability to provide crucial insights for the design phase with a high level of reliability. This level of accuracy, limited to the discussed parameters, is comparable to that obtained from both numerical models. However, the analytical model offers a significant advantage in terms of computational burden. Table 8 presents the results regarding computational load, considering both Time Complexity (calculation duration) and Storage Cost (data storage requirements), in comparison to the numerical simulations. The ratio of the analytical model’s Storage Cost to the OpenFOAM numerical model’s is on the order of 10^{-3} , while the computational time ratio is

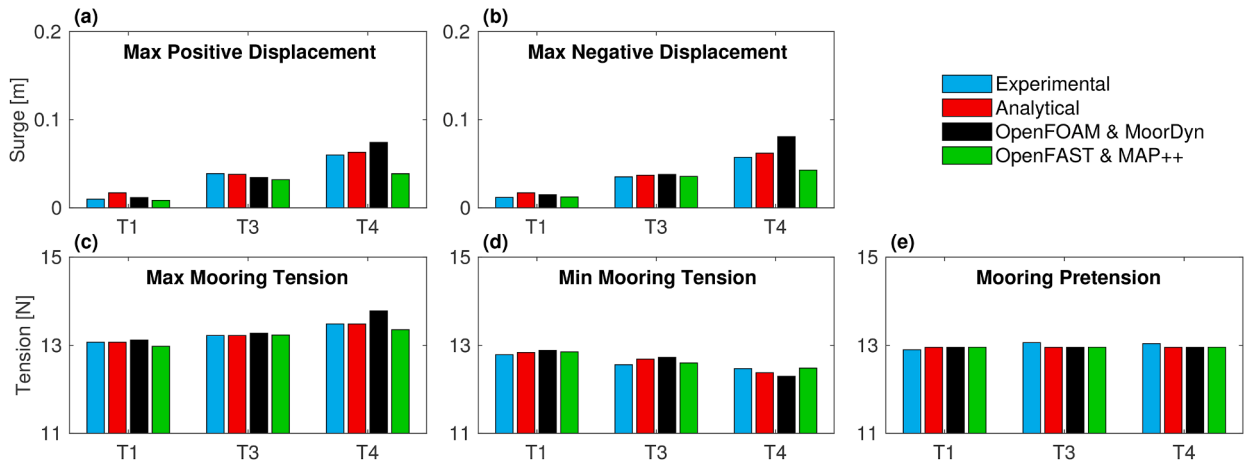


Fig. 14. Comparison of key characteristic values obtained for the three selected tests (T1, T3 and T4), considering experimental results, analytical model predictions, and numerical simulations. Specifically, the analysis examines maximum positive (a) and maximum negative (b) displacements. For mooring line tensions, the comparison includes the maximum (c) and minimum (d) values, along with the pretension (e).

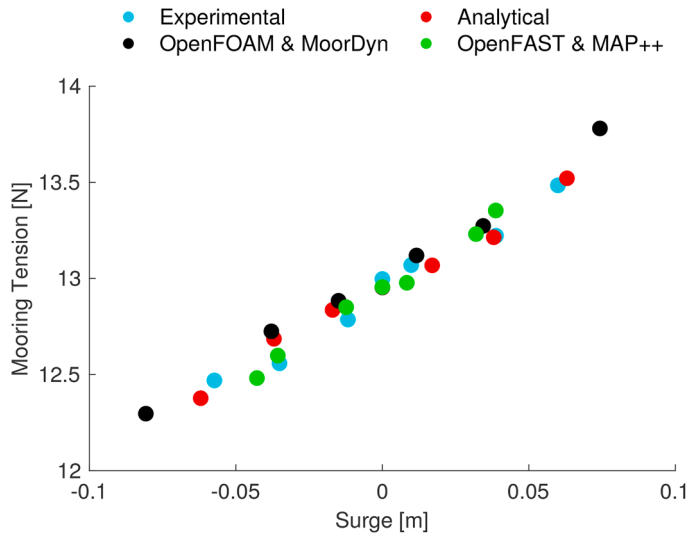


Fig. 15. Scatter plot of the tension-displacement relationship for the three selected tests (T1, T3 and T4), obtained from time-domain simulations. The plotted data include maximum and minimum displacement values along with the corresponding maximum and minimum forces, as well as the zero-displacement condition associated with the initial pretension. Experimental, analytical, and numerical results are compared, highlighting their respective force-displacement relationships.

Table 7

Comprehensive quantitative evaluation of the analytical model’s accuracy using performance metrics such as Mean Absolute Error (MAE), Mean Absolute Percentage Error (MAPE), Root Mean Square Error (RMSE), and the coefficient of determination (R^2), alongside a comparison with the same evaluation performed for the numerical models.

	Analytical		OpenFOAM & MoorDyn		OpenFAST & MAP++	
	Surge	Mooring Tension	Surge	Mooring Tension	Surge	Mooring Tension
MAE	0.0033	0.0515	0.0071	0.1253	0.0065	0.0577
MAPE	0.9025	0.0107	3.4158	0.0723	3.4158	0.0234
RMSE	$1.64 \cdot 10^{-5}$	0.0044	$1.13 \cdot 10^{-4}$	0.0231	$1.01 \cdot 10^{-4}$	0.0048
R^2	0.9934	0.9635	0.9826	0.9288	0.9804	0.9762

Table 8

Evaluation of the computational efficiency of the analytical model in terms of Time Complexity and Storage Cost, providing a detailed comparison with the numerical model. This assessment focuses on quantifying the processing time and memory requirements of both models, providing a clear comparison of their computational demands.

Computational Burden	Storage Cost [GB]	Time Complexity [s]	
T1	Analytical	0.36	0.24
	OpenFOAM & MoorDyn	123	$7.05 \cdot 10^4$
	OpenFAST & MAP++	0.58	63.79
T3	Analytical	0.48	0.18
	OpenFOAM & MoorDyn	122	$9.09 \cdot 10^4$
	OpenFAST & MAP++	0.56	53.58
T4	Analytical	0.36	0.19
	OpenFOAM & MoorDyn	124	$7.91 \cdot 10^4$
	OpenFAST & MAP++	0.57	54.14

on the order of 10^{-6} . Although the computational cost of the analytical model is comparable to, yet lower than, that of OpenFAST, it still offers significant advantages. This analytical model requires far fewer parameters than any other numerical model, thereby reducing both the uncertainties and the time associated with implementation.

3.3. Applicability and limits

Based on the results presented and discussed in the previous sections, this section addresses both the applicability range and the limitations of the analytical formulation proposed in this work. The proposed Linearized SDoF analytical model provides quantitatively reliable results in terms of translational displacements of the structure and tensions in the mooring lines, with a minimum computational burden, both in terms of time and resources. These results highlight several advantages compared to more complex methods, such as experimental campaigns, fully coupled numerical approaches, and other widely used numerical tools. These considerations help to clearly define the applicability domain of the present formulation.

Certainly, experimental methods remain an essential tool for studying complex and nonlinear phenomena, as they allow for direct and integrated observation of fluid-structure interaction. However, as it has been ascertained in the conducted wave-tank experiments (Tomasichio et al., 2020; Russo et al., 2021), these approaches present significant limitations, including high costs, long execution times, limited availability of test facilities, the difficulty of identifying adequate measuring instruments, and challenges in accurately reproducing scaled phenomena. These factors often reduce their practical effectiveness, particularly in the preliminary design phases. To overcome these limitations, fully coupled numerical models currently represent a valuable alternative. They allow for the detailed simulation of complex configurations and offer greater flexibility compared to physical testing. However there are some critical issues with their application. These models require the definition of numerous input parameters and careful calibration based on experimental data, which makes them demanding in terms of both time and computational resources. Moreover, in the preliminary design phase, the absence of prior information on the structural response, often combined with a lack of experimental data for model validation, necessitates the execution of a large number of numerical simulations to achieve an adequate level of modeling reliability, with a consequent increase in time, and thus costs and management complexity. Nevertheless, there are some numerical methods and software alternatives to fully coupled CFD/FSI simulations that allow numerical analysis to be performed in significantly less time. However, the modeling effort required to properly set up simulations in such software is by no means straightforward. For example, with Orcaflex, which is one of the most widely used and established software packages in the offshore wind industry, considerable attention must be paid to selecting the most appropriate mooring line model and its discretization, determining the number of finite elements for the representation of the floater, assigning the correct drag and inertia coefficients for each element, and so forth (Lauria et al., 2024b). OpenFAST, another of the most widely used software programmes, also requires a comprehensive and detailed set of input parameters, which, in some cases, may necessitate the use of auxiliary tools for their definition. The selection of these parameters greatly affects the accuracy of the results and often requires calibrations and sensitivity analysis. These activities introduce inherent uncertainty into the modeling process, without proper validation, and increase the overall modeling effort. In this context, the proposed analytical method emerges as a particularly advantageous solution. The analytical model proposed streamlines the necessary input, thereby minimising the risk of errors associated with inaccurate modelling choices. This feature is especially beneficial during the preliminary design stages, when precise calibration data is frequently unavailable and effective time and cost management is paramount. For example, in the design of a mooring system, the use of this analytical approach would allow for rapid and robust estimation of platform displacements and line tensions, providing crucial preliminary information without the immediate need to implement complex models. Moreover, it can be employed to conduct parametric studies, providing a rapid and comprehensive evaluation of how variations in the mooring system's configuration and properties affect the platform's translational displacements and mooring line forces. Furthermore, the analytical method not only serves as valuable support during the initial design phase but also finds applicability as a complementary tool to numerical models and experimental tests. The same advantages previously outlined can be leveraged in the design of experimental campaigns. The analytical model can support the design and rapid parameterization

of truncated mooring configurations for experimental testing, enabling efficient assessment and calibration of model-scale setup. It guarantees that model-scale tests are dynamically representative and substantially reduces uncertainties associated with mooring line truncation and scaling effects. Finally, this analytical formulation can serve as a useful reference for the verification and validation of numerical results, especially in cases where experimental data are unavailable, as often occurs with innovative or non-standardized configurations.

The accuracy and reliability of the results obtained from an analytical formulation depend strictly on the operating conditions under which the model assumptions remain valid. In particular, the analytical model proposed in this work is not applicable in shallow water and for short waves, as under these conditions Airy wave theory is no longer valid. Since the Morison Equation in its relative velocity formulation for a body moving in an oscillatory flow has been adopted, the present formulation is also unsuitable for structures whose diameter is not significantly smaller than the wavelength, where diffraction effects cannot be neglected. The assumption of regular waves is a common simplification in analytical models, employed to simplify the governing equations and maintain computational efficiency. To ensure engineering relevance, regular waves are parameterized using site-specific characteristic values, such as the significant wave height and period. This approach effectively captures the first-order energy content of the sea state, providing a rapid estimate of the structural response. However, nonlinear effects induced by spectral irregularities, second-order sum-frequency effects, and accurate prediction of viscous damping are not captured by this simplification.

Although the present work focuses on the Surge DoF, the proposed analytical formulation is a SDoF translational system solved in the time domain, offering conceptual flexibility for the analysis of horizontal-plane displacements. The methodology assumes that the complex environmental forces induced by wave action can be represented by a single equivalent unidirectional force. This simplification enables the analysis to the Sway direction, considering both the wave force direction and the mooring system stiffness contributions along the selected axis. It should be noted that, in the present model, each horizontal translational displacement is accompanied by a geometrically imposed linear rotation, Pitch or Roll, depending on the considered DoF. As this rotation is not a true dynamic DoF, the simplification is valid only for small displacements and rotations. Consequently, the model does not capture the actual dynamic coupling between translational and rotational motions, and it cannot accurately predict coupled natural periods or the complete coupled dynamic response. For the same reason, the model is not suitable for waves acting in oblique or non-principal directions, as such loading would activate dynamic coupling terms that are absent in the proposed formulation. Furthermore, as a unidirectional SDoF system, the model does not account for Yaw motion. The omission of this torsional DoF, particularly relevant under oblique or misaligned wave conditions, prevents the evaluation of out-of-plane effects and precludes accurate prediction of the associated effects in mooring lines tensions. For these reasons, the present analytical model is not suitable for the analysis of extreme waves, extreme loads or, more generally, for conditions in which the structure experiences responses beyond the small-displacement regime. Under such circumstances nonlinear effects and significant coupling among the DoF arise, and the mooring system itself enters a nonlinear domain, with possible phenomena such as slack and snap loads, which cannot be considered with the present analytical formulation.

It should be emphasized that the proposed analytical formulation, is not intended to replace more sophisticated methods, as experimental approaches and numerical models possess unmatched power and an indispensable role. However, the simplicity and rapid applicability of the proposed analytical method, combined with the reliability of the results and its low computational burden, underscore its potential as a complementary tool to support and improve the early-stage design process. It allows to address some fundamental challenges associated with more established methodologies while supporting and informing more advanced analysis.

4. Conclusions

The design of mooring systems for FOWTs presents a complex challenge, requiring a balance between structural integrity and economic efficiency. This context calls for integrated approaches that combine experimental testing, advanced numerical modeling, and analytical solutions. Although less commonly explored, analytical methods offer significant potential to enhance the design process by reducing time, cost, and error margins, while also supporting the validation of experimental and numerical data. This study presents a SDoF analytical method for calculating the dynamic characteristics of spar-type FOWTs, with a particular focus on translational displacements and tensions in the mooring lines under hydrodynamic loads. While Morison-based formulations and linear mooring assumptions are well established in offshore engineering, in the present work, a closed-form solution that accurately predicts translational displacements and mooring line tensions at the fairlead point is derived. In particular, the present work has been formulated with reference to the surge DoF; however, by considering waves acting along the sway direction together with the corresponding mooring system stiffness in the same direction, the translational sway displacement and the resulting mooring tensions can also be evaluated. The model, implemented in Matlab R2022a, was applied attempting to simulate a scale model of a FOWT previously experimentally investigated with wave tank tests. The analytical results were validated through comparisons with experimental data and a performance analysis and evaluation was conducted with reference to numerical simulations performed in OpenFOAM coupled with MoorDyn and OpenFAST coupled with MAP++.

The proposed analytical model has demonstrated a strong capability to accurately capture the dynamic characteristics of the system, including stiffness and damping properties, as well as to effectively represent the hydrodynamic forces acting on the structure, despite the simplification to a Linearized SDoF system. Frequency-domain analysis confirms a high level of agreement between the analytical and experimental results regarding both the forcing frequency and the system's response frequency, highlighting the model's ability to predict fundamental dynamic behavior. Moreover, time-domain analysis further validates the model's accuracy, showing that it reliably reproduces the dynamic response of the structure, both in terms of displacement in the analyzed DoF and mooring line tensions.

Focusing on key design parameters, such as maximum and minimum displacements and mooring line tensions, the analytical model has demonstrated a high level of accuracy in their estimation. Furthermore, it effectively captures the relationship between displacements and mooring tensions, accurately reflecting the linear trend observed in the experimental data across the entire test set. This confirms the model's reliability in representing the structural response.

A final yet equally fundamental aspect is that the analytical model delivers results comparable to advanced numerical simulations across all key aspects, including dynamic characteristics, frequency response, time-domain behavior, and key design parameters, while requiring significantly fewer computational resources in terms of both storage cost and time complexity. This approach serves as a valuable tool in the early stages of design, enabling the rapid identification of key parameters to ensure both performance and safety while simultaneously reducing costs and time. Although it cannot replace more detailed numerical or experimental methods, the model proves valuable for conducting initial parametric analysis, planning experimental campaigns, and calibrating numerical simulations.

The results presented in this study highlight the significant potential of simplified analytical models as effective tools to streamline and optimize the preliminary design process. The proposed formulation offers a valuable balance between accuracy and practicality, providing rapid and reliable estimations with minimal computational effort and input requirements. These features make it particularly useful in the early design phases, where time, cost, and limited data availability are critical factors. Although the model's accuracy is inherently linked to the validity of its underlying assumptions, as previously discussed, it represents a powerful support tool across the design process and for various applications, including parametric analysis, preliminary mooring system assessments, experimental planning, and numerical model verification. The purpose of the present analytical model is not to replace advanced numerical tools, but to complement them, providing valuable support in the preliminary design phases and contributing to the optimization of the overall design process.

Considering the analytical model's demonstrated potential, future efforts will be devoted to extending its applicability and consolidating its role in early-stage design support. Considering the importance of assessing the effects of wave-wind-structure interaction during the design process and the need to represent site-specific conditions, future developments will aim to integrate aerodynamic loads and irregular wave conditions enabling a more comprehensive evaluation of the offshore system response and a more accurate investigation of nonlinear dynamic effects. Further research will also focus on broadening the model's applicability to a wider range of mooring system configurations and floating platform designs. Moreover, expanding the analytical formulation to account for multiple DoF, while retaining its computational efficiency, represents a promising direction to further enhance the model's flexibility and practical value.

CRedit authorship contribution statement

Pierpaolo Loprieno: Writing – review & editing, Writing – original draft, Visualization, Validation, Software, Methodology, Formal analysis, Conceptualization; **Fabio Rizzo:** Writing – review & editing, Validation, Supervision, Resources; **Elisa Leone:** Writing – review & editing, Investigation, Data curation; **Dora Foti:** Writing – review & editing, Supervision, Resources; **Giuseppe Roberto Tomasicchio:** Supervision, Resources, Funding acquisition; **Agostino Lauria:** Writing – review & editing, Validation, Supervision, Resources, Conceptualization.

Data availability

Data will be made available on request.

Declaration of competing interest

The authors declare that they have no known competing financial interests or personal relationships that could have appeared to influence the work reported in this paper.

Acknowledgements

The present research was funded by the European Union - Next Generation EU through the grant of the project PRIN 2022 titled “NonlinEar Phenomena in floaTing offshore wind tUrbiNEs (NEPTUNE)”, Project code: 2022W7SKTL.

Supplementary material

Supplementary material associated with this article can be found in the online version at [10.1016/j.jfluidstructs.2025.104475](https://doi.org/10.1016/j.jfluidstructs.2025.104475).

Appendix A. Analytical model details

The detailed calculations related to the analytical model presented in this paper are provided in this Appendix. Specifically [A.1](#) outlines the calculation of the structural stiffness component of the mooring lines, while [A.2](#) presents the formulation of the analytical expression for the center of pressure. [A.3](#) details the procedure used to establish the time-dependent solution of the displacements, and [A.4](#) provides the closed-form expression for computing the deformed length of the mooring lines.

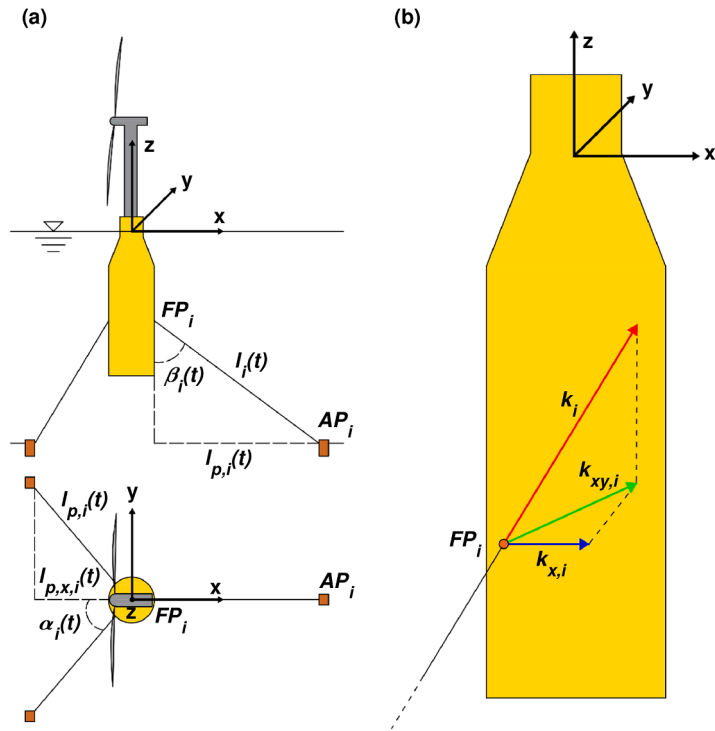


Fig. A.1. Schematic representation of the characterization parameters of the mooring system in the proposed analytical model, presented in the vertical xz and horizontal xy planes (a). In panel (b), the decomposition of the axial stiffness characteristic is illustrated, emphasizing its components in the xy plane and along the x direction.

A.1. Structural stiffness components of mooring lines

In this Appendix, the reader will find a comprehensive exposition of the analytical method for calculating the stiffness contribution of the mooring lines related to the considered degree of freedom. Let's consider the generic case shown in the Fig. A.1.

Let's denote by $FP_i = (x_{FP,i}, y_{FP,i}, z_{FP,i})$ the coordinates of fairlead points and by $AP_i = (x_{AP,i}, y_{AP,i}, z_{AP,i})$ those of the anchorage points with respect to the fixed reference system. A generic mooring system has mooring lines with two inclinations, one with respect to the x -axis and one with respect to the z -axis, $\alpha_i(t)$ and $\beta_i(t)$, both varying in time according to the displacements undergone by the structure. Denoting by $l_{p,i}(t)$ the projection of the generic cable on the horizontal plane xy and by $l_{p,x,i}(t)$ its projection on the x -axis, it is possible to define

$$\cos \alpha_i(t) = l_{p,x,i}(t) / l_{p,i}(t), \quad \cos \beta_i(t) = l_{p,i}(t) / l_i(t). \quad (A.1)$$

It is now possible to derive the contribution along the x axis of the axial stiffness of each mooring line through simple geometric considerations. In particular, it is possible to calculate the contribution along x of the elastic and geometric stiffness of each cable respectively as

$$k_{El,x,i}(t) = (EA / l_{0,i}) \cos \alpha_i(t) \cos \beta_i(t), \quad k_{G,x,i}(t) = (T_i(t) / l_i(t)) \cos \alpha_i(t) \cos \beta_i(t). \quad (A.2)$$

Consequently, the overall stiffness of the i -th mooring line is equal to:

$$k_{x,i}(t) = k_{El,x,i}(t) + k_{G,x,i}(t). \quad (A.3)$$

A.2. Analytical expression of the center of pressure

This Appendix shows the reader the method for calculating the centre of pressure at which the resultant of the hydrodynamic loads, calculated according to Eq. (11), will be applied. According to the assumptions of the Morison equation, the fluid motion around the structure is linear, making it valid for linear waves described by Airy wave theory. The free surface elevation of such waves can be expressed using the following equation

$$\eta(t) = \frac{H}{2} \cos(\kappa x - \Omega t + \Phi), \quad (A.4)$$

where H represents the wave height, $\kappa = \Omega^2 / g = 2\pi / \lambda$ is the wave number, with g gravity acceleration, $\Omega = 2\pi / T$ wave angular frequency, T wave period; Φ is the phase shift, which describes the temporal and spatial positioning of the wave form relative to the

chosen coordinate system and x denotes the spatial coordinate or the reference horizontal position within that system. According to wave particle kinematics, for the defined wave, the distribution of the horizontal velocity and the horizontal acceleration of wave particles can be expressed respectively as

$$u_x(z, t) = \Omega \frac{H}{2} e^{\kappa z} \cos(\kappa x - \Omega t + \Phi), \quad \dot{u}_x(z, t) = \Omega^2 \frac{H}{2} e^{\kappa z} \sin(\kappa x - \Omega t + \Phi), \tag{A.5}$$

both time-varying and depending on the depth z . Considering $F_{x,eq,z}(z, t)$ the actual load distribution of $F_{x,eq}(t)$ (Eq. (11)) and thus its variability along z

$$F_{x,eq,z}(z, t) = \rho C_m V_w \dot{u}_x(z, t) + \frac{1}{2} \rho C_d A_w u_x(z, t) |u_x(z, t)|, \tag{A.6}$$

it is possible to identify the coordinate z_{CP} as follows

$$z_{CP} = \frac{1}{T_a} \int_0^{T_a} \left[\frac{\int_{-d}^0 z F_{x,eq,z}(z, t) dz}{\int_{-d}^0 F_{x,eq,z}(z, t) dz} \right] dt, \tag{A.7}$$

with T_a analysis time considered.

A.3. Establishment of the time-dependent solution

The purpose of this Appendix is to present to the reader the analytical procedure that was utilised in order to determine the equation of motion and its time-dependent solution. This procedure is based on the assumptions that underpin the present analytical model. In Section 2.1.1, the mass terms of the structure, denoted by m_x and the structural damping, denoted by c_x were defined. The equivalent stiffness of the system, denoted by $k_x(t)$ (Eq. (4)), was calculated with reference to the degree of freedom considered, i.e. horizontal translation along the x axis, as detailed in A.1. In Section 2.1.2, on the other hand, the resultant of the hydrodynamic loads applicable to the centre of pressure CP (defined in A.2) was defined in Eq. (6). Placing these terms within the equation of motion SDoF, and taking into account the approximate form of F_{Drag} (Eq. (10)), we derive

$$m_x \ddot{p}_{x,CP}(t) + c_x \dot{p}_{x,CP}(t) + k_x(t) p_{x,CP}(t) = \rho V_w \dot{u}_x(t) + \rho C_a V_w (\dot{u}_x(t) - \ddot{p}_{x,CP}(t)) + \frac{1}{2} \rho C_d A_w (u_x(t) - \dot{p}_{x,CP}(t)) |u_x(t) - \dot{p}_{x,CP}(t)|; \tag{A.8}$$

rearranging the terms, the following equation is obtained

$$(m_x + \rho C_a V_w) \ddot{p}_{x,CP}(t) + (c_x + \rho C_d A_w |u_x(t)|) \dot{p}_{x,CP}(t) + k_x(t) p_{x,CP}(t) = \rho C_m V_w \dot{u}_x(t) + \frac{1}{2} \rho C_d A_w u_x(t) |u_x(t)|. \tag{A.9}$$

In consideration of the definitions of equivalent mass and damping of the system, in conjunction with the linearisation of the second term of the equation (Eq. (12)) presented in Section 2.1.2, the derivation of Eq. (14) becomes feasible. This differential equation is known to be solved as follows

$$p_{x,CP}(t) = e^{(-\beta t)} [C_1 \sin(\omega_d(0)t) + C_2 \cos(\omega_d(0)t)] + p_p(t). \tag{A.10}$$

which consists of a transient part related to the characteristics of the structure, the general integral, and a stationary part related to the forcing, the particular integral $p_p(t)$. Consequently, the particular integral takes the following form:

$$p_p(t) = \sum_{j=1}^q p_j^{(a_j)}(t) + \sum_{j=1}^q p_j^{(b_j)}(t), \tag{A.11}$$

where

$$p_j^{(a_j)}(t) = \frac{a_j}{k_x(t)} X_j(t) \sin(j\Omega t - \phi_j), \quad p_j^{(b_j)}(t) = \frac{b_j}{k_x(t)} X_j(t) \cos(j\Omega t - \phi_j). \tag{A.12}$$

The term $X_j(t)$ will be expressed as

$$X_j(t) = \left[\sqrt{\left(1 - j^2 \frac{\Omega^2}{\omega_n^2}\right)^2 + \left(2j\zeta(t) \frac{\Omega}{\omega_n}\right)^2} \right]^{-1}, \tag{A.13}$$

variable over time according to $\zeta(t)$, while ϕ_j , which represents the phase shift of the structure's response and does not vary over time, is equal to

$$\phi_j = \arctan \left(\frac{2j\zeta(0) \frac{\Omega}{\omega_n}}{1 - \left(j \frac{\Omega}{\omega_n}\right)^2} \right). \tag{A.14}$$

Substitute the form of the particular integral just determined into the equation above, obtaining Eq. (15). Let the initial conditions of problem C.I. be set equal to

$$C.I. = \begin{cases} p_{x,CP}(0) = 0 \\ \dot{p}_{x,CP}(0) = 0 \end{cases}. \tag{A.15}$$

These conditions are possible because it is assumed that at $t = 0$ the structure has reached the equilibrium position and that this condition is only subsequently disturbed by the hydrodynamic force in the surge direction. By imposing the *C.I.* it is possible to determine the two constants C_1 and C_2 which will have the following forms

$$C_1 = \left[\beta C_2 - \sum_{j=1}^q j\Omega \frac{a_j}{k_x(0)} X_j(0) \cos(-\phi_j) + \sum_{j=1}^q j\Omega \frac{b_j}{k_x(0)} X_j(0) \sin(-\phi_j) \right] / \omega_d(0), \tag{A.16}$$

$$C_2 = - \sum_{j=1}^q \frac{a_j}{k_x(0)} X_j(0) \sin(-\phi_j) - \sum_{j=1}^q \frac{b_j}{k_x(0)} X_j(0) \cos(-\phi_j). \tag{A.17}$$

A.4. Closed form expressions of the deformed length of the mooring lines

In this Appendix, readers are instructed on how to calculate the deformed length, instant by instant, based on the displacements of the fairlead point. Given an instant t , undergoing a displacement $p_{x,FP,i}(t)$, obtained in accordance with Eq. (21), it is possible to calculate the projection $l_{p,x,i}(t)$ on the x axis of the length of the deformed mooring line as

$$l_{p,x,i}(t) = \left| x_{AP,i} - (x_{FP,i} + p_{x,FP,i}(t)) \right|. \tag{A.18}$$

Recalling that, for the assumptions of the SDoF model, displacements y and z are null, through simple geometric considerations it is possible to derive its projection on the xy plane

$$l_{p,i}(t) = \sqrt{(l_{p,x,i}(t))^2 + |y_{AP,i} - y_{FP,i}|^2}, \tag{A.19}$$

and thus achieve the deformed length of the mooring lines caused by displacement

$$l_i(t) = \sqrt{(l_{p,i}(t))^2 + |z_{AP,i} - z_{FP,i}|^2}. \tag{A.20}$$

Definition of $l_{p,i}(t)$, $l_{p,x,i}(t)$, FP_i and AP_i are provided in A.1 as well as a graphical representation in Fig. A.1.

Appendix B. Domain height sensitivity analysis

In this Appendix, the results of a sensitivity analysis are reported to verify that the selected height of the computational domain for the air phase does not adversely affect the numerical results.

The upper section of the computational domain representing the air phase was set to a height of 4 m, approximately 1.7 times the hub height (rounded up). This provides a vertical clearance of 1 m above the tip of the blades.

To assess whether this height is sufficient to capture the free-surface evolution accurately, two additional heights were considered: 4.875 m (+22%) and 5.75 m (+44%) (Fig. B.1).

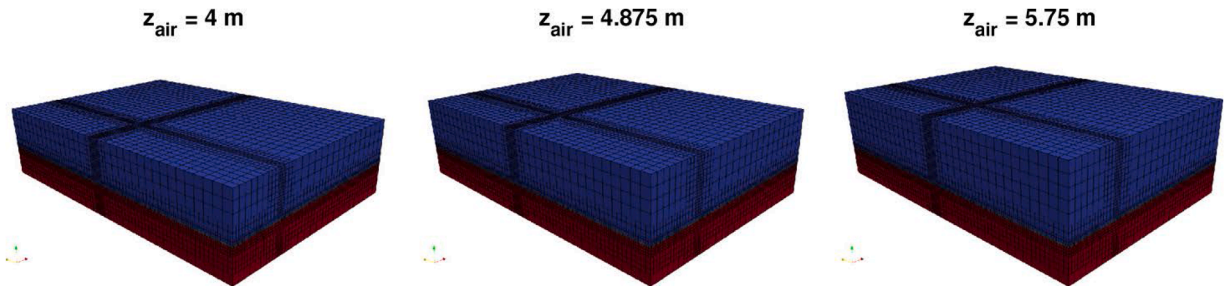


Fig. B.1. Computational domains representing the air phase with three different heights considered in the sensitivity analysis. The baseline domain has a height of 4 m, while the other two domains are increased by 22 % (4.875 m) and 44 % (5.75 m). These variations were used to evaluate the influence of domain height on the accurate capture of the free-surface elevation.

For each numerical test case (T1, T3, and T4), the free-surface elevations obtained with the three domain heights were compared. As shown in Fig. B.2, further variations in domain height produce virtually no change. Table B.1 reports the corresponding MAPE values calculated over the entire time history of the free-surface elevation. The maximum MAPE observed is only 0.0236%, confirming the negligible effect of increasing the domain height. Since aerodynamic forces were not considered and a 4 m domain height is sufficient for proper wave development, this configuration was selected as a balanced choice, providing both accurate numerical results and reduced computational cost.

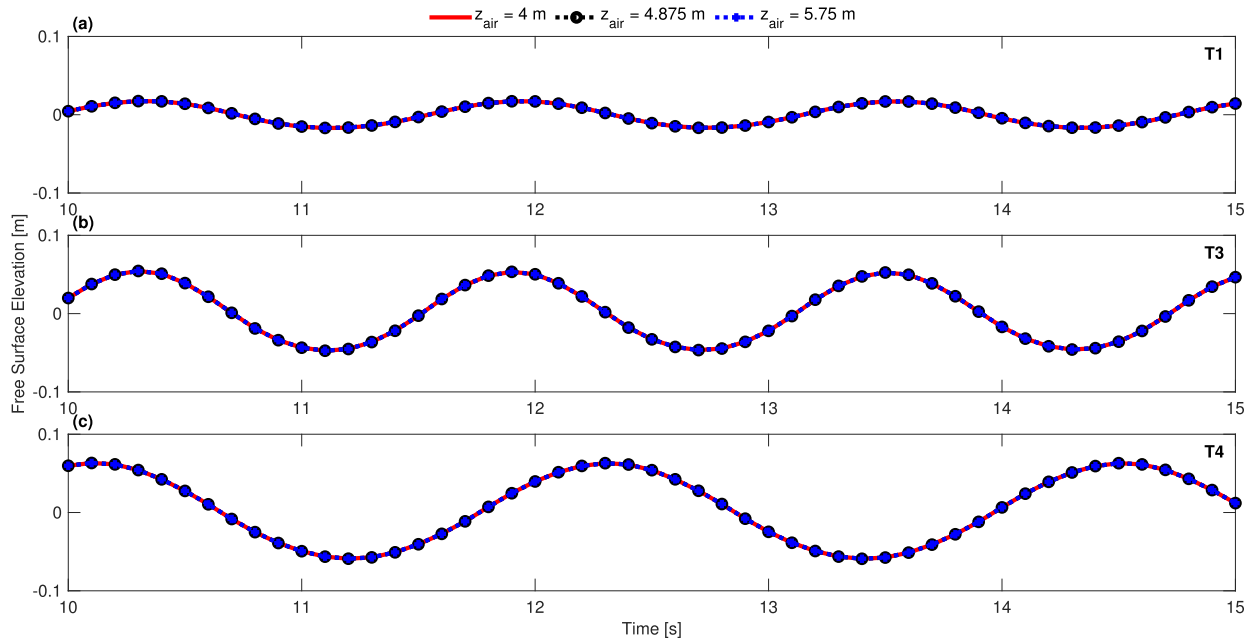


Fig. B.2. Time histories of the free-surface elevation for test cases T1, T3, and T4 ((a), (b), and (c), respectively) computed with the three domain heights. The results show that further increases in domain height have a negligible effect on the free-surface evolution.

Table B.1

Mean Absolute Percentage Error (MAPE) of the free-surface elevation time histories for test cases T1, T3, and T4, calculated for the domain heights of 4.875 m and 5.75 m with respect to the reference domain height of 4 m. The results confirm that increasing the domain height produces negligible differences, with a maximum MAPE of 0.0236 %.

MAPE	T1	T3	T4
$z_{air} = 4.875m$	0.0000	0.0100	0.0183
$z_{air} = 5.750m$	0.0028	0.0153	0.0236

References

Aboutalebi, P., Garrido, A.J., Garrido, I., Nguyen, D.T., Gao, Z., 2024. Hydrostatic stability and hydrodynamics of a floating wind turbine platform integrated with oscillating water columns: a design study. *Renew. Energy* 221, 119824.

Afridi, S.K., Koondhar, M.A., Jamali, M.I., Alaas, Z.M., Alsharif, M.H., Kim, M.-K., Mahariq, I., Touti, E., Aoudia, M., Ahmed, M., 2024. Winds of progress: an in-depth exploration of offshore, floating, and onshore wind turbines as cornerstones for sustainable energy generation and environmental stewardship. *IEEE Access* . 12, 66147-66166.

Al-Solihat, M.K., Nahon, M., 2016. Stiffness of slack and taut moorings. *Ship. Offshore Struct.* 11 (8), 890–904.

Al-Solihat, M.K., Nahon, M., 2018. Flexible multibody dynamic modeling of a floating wind turbine. *Int. J. Mech. Sci.* 142, 518–529.

Ali, A., Shi, W., Wang, S., Zhai, H., Haider, R., Leng, S., Li, X., Han, X., 2025. Dynamic analysis of a tetraspar floating offshore wind turbine with different tendons failure scenario. *Ocean Eng.* 323, 120607.

Aliyar, S., Ducrozet, G., Bouscasse, B., Bonnefoy, F., Sriram, V., Ferrant, P., 2022. Numerical coupling strategy using HOS-openFOAM-moordyn for OC3 hywind SPAR type platform. *Ocean Eng.* 263, 112206.

Amaral, G.A., Pesce, C.P., Franzini, G.R., 2022. Mooring system stiffness: a six-degree-of-freedom closed-form analytical formulation. *Mar. Struct.* 84, 103189.

Amaral, G.A., Pesce, C.P., Franzini, G.R., 2024. Shared mooring system equivalent stiffness: a closed-form analytical formulation with an application to fowfs. Available at SSRN 4711708.

Barooni, M., Ashuri, T., Velioglu Sogut, D., Wood, S., Ghaderpour Taleghani, S., 2022. Floating offshore wind turbines: current status and future prospects. *Energies* 16 (1), 2.

Bian, J., Wan, L., Yang, Y., Li, S., Hao, J., Xin, J., Zhang, C., 2025. Dynamic response analysis of alternative mooring system designs for a 15MW floating wind turbine with an emphasize on different limit states. *Ocean Eng.* 315, 119787.

Borg, M., Collu, M., 2015. Offshore floating vertical axis wind turbines, dynamics modelling state of the art. part III: hydrodynamics and coupled modelling approaches. *Renew. Sustain. Energy Rev.* 46, 296–310.

Chen, H., Hall, M., 2022. Cfd simulation of floating body motion with mooring dynamics: coupling moordyn with openfoam. *Appl. Ocean Res.* 124, 103210.

Chen, P., Chen, J., Hu, Z., 2020. Review of experimental-numerical methodologies and challenges for floating offshore wind turbines. *J. Mar. Sci. Appl.* 19, 339–361.

Commission, E., 2021. Fit for 55 Package: Delivering the EU’s 2030 Climate Target on the Way to Climate Neutrality. Technical Report.

Coraddu, A., Oneto, L., Walker, J., Patryniak, K., Prothero, A., Collu, M., 2024. Floating offshore wind turbine mooring line sections health status nowcasting: from supervised shallow to weakly supervised deep learning. *Mech. Syst. Signal Process.* 216, 111446.

- Coughlan, K., Davis, M., Westgate, Z., Lee, J., Arwade, S., Martin, B., DeGroot, D., 2025. Design and analysis of shared anchor layouts for floating wind farms in deep waters. *Ocean Eng.* 320, 120208.
- Dean, R.G., Dalrymple, R.A., 1991. *Water Wave Mechanics for Engineers and Scientists*. Vol. 2. World Scientific Publishing Company.
- DNV, 2017. DNV-RP-F205: Global Performance Analysis of Deepwater Floating Structures. Technical Report. DNV. Høvik, Norway. Recommended Practice, April 2017.
- DNV, 2021a. DNV-RP-C205: Environmental Conditions and Environmental Loads. Technical Report. DNV. Høvik, Norway. Recommended Practice, April 2021.
- DNV, 2021b. DNV-ST-E301: Position Mooring. Technical Report DNV-ST-E301. DNV. Edition July 2021.
- Dodaran, A.A., Park, S.-K., 2012. Development of design static property analysis of mooring system caisson for offshore floating wind turbine. *Int. J. Ocean Syst. Eng.* 2 (2), 97–105.
- European Commission, 2022. REPowerEU Plan: Joint European Action for More Affordable, Secure and Sustainable Energy. Technical Report.
- European Union, 2018. Directive (EU) 2018/2001 of the European Parliament and of the Council on the Promotion of the Use of Energy from Renewable Sources (Recast). Technical Report.
- Gharechae, A., Negahdari, M.R., 2022. Semi-analytical study of the first order horizontal force induced by oblique waves on the array of circular columns of offshore wind turbines equipped with permeable cylinders. *Ocean Eng.* 261, 112043.
- Goupee, A.J., Koo, B.J., Kimball, R.W., Lambrakos, K.F., Dagher, H.J., 2014. Experimental comparison of three floating wind turbine concepts. *J. Offshore Mech. Arct. Eng.* 136 (2), 020906.
- Hao, S., Zhang, X., Yu, Y., Wang, B., Bo, X., 2025. Mooring failure analysis of semisubmersible floating offshore wind turbines considering mooring redundancy at each azimuth angle. *J. Mar. Sci. Eng.* 13 (2), 360.
- Haritos, N., 2007. Introduction to the analysis and design of offshore structures—an overview. *Electron. J. Struct. Eng.* (1), 55–65.
- He, C., Sun, T., Zhang, Z., Liu, H., Wang, C., Wang, J., 2025. Numerical investigation on the second-order sum-frequency wave forces induced mooring fatigue of a 15 MW TLP FOWT. *Ocean Eng.* 322, 120463.
- Hegseth, J.M., Bachynski, E.E., 2019. A semi-analytical frequency domain model for efficient design evaluation of spar floating wind turbines. *Mar. Struct.* 64, 186–210.
- Høeg, C.E., Zhang, Z., 2023. A semi-analytical hydrodynamic model for floating offshore wind turbines (FOWT) with application to a FOWT heave plate tuned mass damper. *Ocean Eng.* 287, 115756.
- Hong, S., McMorland, J., Zhang, H., Collu, M., Halse, K.H., 2024. Floating offshore wind farm installation, challenges and opportunities: a comprehensive survey. *Ocean Eng.* 304, 117793.
- Ishihara, T., Zhang, S., 2019. Prediction of dynamic response of semi-submersible floating offshore wind turbine using augmented morison's equation with frequency dependent hydrodynamic coefficients. *Renew. Energy* 131, 1186–1207.
- ITTC, 2021a. Recommended procedures and guidelines - 7.5-02-07-03.1 floating offshore platform experiments (7.5-02-07-03.1), 12.
- ITTC, 2021b. Recommended procedures and guidelines - 7.5-02-07-03.16 model construction of offshore systems (7.5-02-07-03.16), 12.
- ITTC, 2021c. Recommended procedures and guidelines - 7.5-02-07-08.8 model tests for offshore wind turbines (7.5-02-07-08.8), 19.
- Jiang, C., el Moctar, O., Paredes, G.M., Schellin, T.E., 2020. Validation of a dynamic mooring model coupled with a RANS solver. *Mar. Struct.* 72, 102783.
- Jiang, Z., 2025. Mooring design for floating wind turbines: a review. *Renew. Sustain. Energy Rev.* 212, 115231.
- Jonkman, J., 2009. Definition of a 5-MW Reference Wind Turbine for Offshore System Development. Technical Report. Technical Report, NREL/TP-500-38060.
- Jonkman, J., 2010. Definition of the Floating System for Phase IV of OC3. Technical Report. Technical Report, NREL/TP-500-47535.
- Kim, Y.J., Charlou, M., Bouscasse, B., Leroy, V., Aliyar, S., Bonnefoy, F., Kim, K.-H., Choi, Y.-M., 2025. High fidelity simulations of a floating offshore wind turbine in irregular waves by coupling openFOAM and openFAST. *Renew. Energy*, 122486.
- Kumar, R., Subhamoy, S., Keprate, A., 2025. Real-time fatigue assessment of floating offshore wind turbine mooring employing sequence-to-sequence-based deep learning on indirect fatigue response. *Ocean Eng.* 315, 119741.
- Lauria, A., Alfonsi, G., 2020. Numerical investigation of ski jump hydraulics. *J. Hydraul. Eng.* 146 (4), 04020012.
- Lauria, A., Loprieno, P., Francone, A., Leone, E., Tomasicchio, G.R., 2024a. Recent advances in understanding the dynamic characterization of floating offshore wind turbines. *Ocean Eng.* 307, 118189.
- Lauria, A., Loprieno, P., Rizzo, F., Severini, A., Foti, D., Leone, E., Francone, A., Tomasicchio, G.R., 2024b. On the effects of wind and operating conditions on mooring line tensions for floating offshore wind turbine. *Appl. Ocean Res.* 152, 104197.
- Lee, C.F., Fjermedal, S., Ong, M.C., 2024. Design and analysis of taut mooring systems for a combined floating offshore wind and wave energy system at intermediate water depth. *Ocean Eng.* 312, 119174.
- Lee, C.F., Fjermedal, S., Ong, M.C., 2025. Design and comparative analysis of mooring systems for a combined wind and wave energy system at intermediate water depth. *J. Ocean Eng. Sci.* 10, 492-508.
- Lee, H., Lee, D.-J., 2019. Effects of platform motions on aerodynamic performance and unsteady wake evolution of a floating offshore wind turbine. *Renew. Energy* 143, 9–23.
- Lei, Z., Wang, X., Zhou, S., Wang, Z., Wang, T., Yang, Y., 2021. A review of research status and scientific problems of floating offshore wind turbines. *Energy Eng.* 119 (1), 123–143.
- Li, C., Chen, P., Deng, S., Wang, S., Cheng, Z., Xiao, L., 2024a. Effects of ballast transfer on modeling and dynamic responses of a 15MW semi-submersible floating wind turbine. *Ocean Eng.* 302, 117581.
- Li, C.B., Zhang, Z., Zhang, J., Li, X., Choung, J., Chen, M., 2024b. Investigation on local mooring stresses of floating offshore wind turbines considering mooring chain geometrical and material nonlinearity. *Ocean Eng.* 312, 119166.
- Lian, Y., Zhong, F., Zheng, J., Chen, W., Ma, G., Wang, S., Yim, S.C., 2023. Effects of mooring line with different materials on the dynamic response of offshore floating wind turbine. *J. Mar. Sci. Eng.* 11 (12), 2302.
- Liang, G., Lopez-Olocco, T., Medina-Manuel, A., Saavedra-Ynocente, L.A., Souto-Iglesias, A., Jiang, Z., 2024. Experimental investigation of two shared mooring configurations for a dual-spar floating offshore wind farm in irregular waves. *Mar. Struct.* 95, 103579.
- Lin, Y.-H., Huang, Y.-R., 2022. Drift simulation of a floating offshore wind turbine with broken mooring lines in a dynamic sea condition. *Ocean Eng.* 266, 112729.
- Liu, Z., Zhao, J., Lin, X., 2024. Effects of mooring line failure on semi-submersible wind turbine and the study of its mitigation measures. *Ocean Eng.* 311, 118889.
- Lozon, E., Lekkala, M.R., Sirkis, L., Hall, M., 2025. Reference mooring and dynamic cable designs for representative US floating wind farms. *Ocean Eng.* 322, 120473.
- Ma, K.-t., Wu, Y., Stolen, S.F., Bello, L., ver der Horst, M., Luo, Y., 2021. Mooring designs for floating offshore wind turbines leveraging experience from the oil & gas industry. In: *International Conference on Offshore Mechanics and Arctic Engineering*. Vol. 85116. American Society of Mechanical Engineers, p. V001T01A031.
- Malta, E.B., Gonçalves, R.T., Matsumoto, F.T., Pereira, F.R., Fajarra, A. L.C., Nishimoto, K., 2010. Damping coefficient analyses for floating offshore structures. In: *International Conference on Offshore Mechanics and Arctic Engineering*. Vol. 49095, pp. 83–89.
- Martin, T., Bihs, H., 2021. A numerical solution for modelling engineering dynamics, including bending and shearing effects, using a geometrically exact beam model. *J. Mar. Sci. Eng.* 9 (5), 486.
- Masciola, M., Jonkman, J., 2013. Development of a Multisegmented, Quasi-Static Cable Model with an Analytical Jacobian for Modeling Floating Offshore Wind Turbines.
- Masciola, M.D., 2025. MAP + +: Mooring Analysis Program. National Renewable Energy Laboratory. <https://www.nrel.gov/wind/nwtc/map-plus-plus>.
- McMorland, J., Collu, M., McMillan, D., Carroll, J., 2022. Operation and maintenance for floating wind turbines: a review. *Renew. Sustain. Energy Rev.* 163, 112499.
- Medina-Manuel, A., Molina Sánchez, R., Souto-Iglesias, A., 2024. Ai-driven model prediction of motions and mooring loads of a spar floating wind turbine in waves and wind. *J. Mar. Sci. Eng.* 12 (9), 1464.
- Meng, H., Liu, Y., Tian, D., Long, K., Han, Z., Su, Y., Sun, K., 2025. Dynamic response of novel floating wind turbine to freak waves during uninterrupted operation. *Renew. Energy* 239, 121984.
- Meng, Q., Hua, X., Chen, C., Zhou, S., Liu, F., Chen, Z., 2022. Analytical study on the aerodynamic and hydrodynamic damping of the platform in an operating spar-type floating offshore wind turbine. *Renew. Energy* 198, 772–788.

- Merz, K.O., Moe, G., Gudmestad, O.T., 2009. A review of hydrodynamic effects on bottom-fixed offshore wind turbines. In: Proceedings of the 28th ASME International Conference on Ocean, Offshore and Arctic Engineering (OMAE). ASME, pp. 927–941.
- National Renewable Energy Laboratory (NREL), 2023. OpenFAST User's Guide. National Renewable Energy Laboratory. Golden, CO, USA. <https://openfast.readthedocs.io>.
- Neisi, A., Ghassemi, H., Iranmanesh, M., 2024. Dynamic response of three different floating platform (OC4, BSS, GVA) using multi-segment mooring system. *Appl. Ocean Res.* 153, 104301.
- Nie, D., Yang, Y., Li, S., Yu, J., Bashir, M., Yin, J., Ren, Y., Hao, J., Wang, F., Liu, Q., et al., 2024. Investigation of mooring breakage impact on dynamic responses of a 15 MW floating offshore wind turbine. *Ocean Eng.* 311, 118996.
- Otter, A., Murphy, J., Pakrashi, V., Robertson, A., Desmond, C., 2022. A review of modelling techniques for floating offshore wind turbines. *Wind Energy* 25 (5), 831–857.
- Patryniak, K., Collu, M., Coraddu, A., 2022. Multidisciplinary design analysis and optimisation frameworks for floating offshore wind turbines: state of the art. *Ocean Eng.* 251, 111002.
- Pesce, C.P., Amaral, G.A., Franzini, G.R., 2018. Mooring system stiffness: a general analytical formulation with an application to floating offshore wind turbines. In: International Conference on Offshore Mechanics and Arctic Engineering. Vol. 51975. American Society of Mechanical Engineers, p. V001T01A021.
- Que, Z., Zou, D., Yang, J., Wei, H., Liu, T., 2025. Effect of mooring failure and wind-wave misalignment on semi-submersible FOWT platform equipped with a novel primary-secondary mooring system. *Ocean Eng.* 326, 120877.
- Ricciardelli, F., Maienza, C., Vardaroglu, M., Avossa, A.M., 2021. Wind energy into the future: the challenge of deep-water wind farms. *Wind Struct.* 32 (4), 321–340.
- Ronge, E., Peyrard, C., Venugopal, V., Xiao, Q., Johanning, L., 2022. The application of semi-analytical diffraction formulas to predict second-order dynamic response of a TLP floating wind turbine in monochromatic waves. In: International Conference on Offshore Mechanics and Arctic Engineering. Vol. 85932. American Society of Mechanical Engineers, p. V008T09A018.
- Rui, S., Zhou, Z., Gao, Z., Jostad, H.P., Wang, L., Xu, H., Guo, Z., 2024. A review on mooring lines and anchors of floating marine structures. *Renew. Sustain. Energy Rev.* 199, 114547.
- Russo, S., Contestabile, P., Bardazzi, A., Leone, E., Iglesias, G., Tomasicchio, G.R., Vicinanza, D., 2021. Dynamic loads and response of a spar buoy wind turbine with pitch-controlled rotating blades: an experimental study. *Energies* 14 (12), 3598.
- Sablok, A., Koo, B., Milante, T., 2024. Efficient design of floating offshore wind turbines. In: International Conference on Offshore Mechanics and Arctic Engineering. Vol. 87851. American Society of Mechanical Engineers, p. V007T09A050.
- Santo, H., Taylor, P.H., Day, A.H., Nixon, E., Choo, Y.S., 2018. Blockage and relative velocity morison forces on a dynamically-responding jacket in large waves and current. *J. Fluid. Struct.* 81, 161–178.
- Sasinthiran, A., Gnanasekaran, S., Ragala, R., 2024. A review of artificial intelligence applications in wind turbine health monitoring. *Int. J. Sustain. Energy* 43 (1), 2326296.
- Schäffer, H.A., Klopman, G., 2000. Review of multidirectional active wave absorption methods. *J. Waterway, Port, Coastal, Ocean Eng.* 126 (2), 88–97.
- Sengupta, D., Pal, S.K., Datta, R., 2017. Hydroelasticity of a 3d floating body using a semi analytic approach in time domain. *J. Fluid. Struct.* 71, 96–115.
- Sharma, S., Nava, V., 2024. Condition monitoring of mooring systems for floating offshore wind turbines using convolutional neural network framework coupled with autoregressive coefficients. *Ocean Eng.* 302, 117650.
- Somoano, M., Blanco, D., Rodríguez-Luis, A., Guanache, R., 2022. Experimental analysis of mooring and power cable dynamics when using elastic string models. In: International Conference on Offshore Mechanics and Arctic Engineering. Vol. 85932. American Society of Mechanical Engineers, p. V008T09A044.
- Subbulakshmi, A., Verma, M., 2024. Dynamic response analysis of a semisubmersible floating offshore wind turbine subjected to mooring line failure under normal and extreme environmental conditions. *Ocean Eng.* 304, 117907.
- Subbulakshmi, A., Verma, M., Keerthana, M., Sasmal, S., Harikrishna, P., Kapuria, S., 2022. Recent advances in experimental and numerical methods for dynamic analysis of floating offshore wind turbines-an integrated review. *Renew. Sustain. Energy Rev.* 164, 112525.
- Tang, H.-J., Ong, M.C., Hsu, T.-W., 2024. Dynamic analysis of a 15 MW semi-taut mooring floating offshore wind turbine at intermediate water depth: investigating mooring line failure under operating and parked conditions. *Ocean Eng.* 312, 119108.
- Tang, H.-J., Yao, H.-C., Ong, M.C., Yang, R.-Y., 2025. Experimental study of a barge-type floating offshore wind turbine under a sequential mooring line failure. *Ocean Eng.* 317, 119999.
- Tang, H.-J., Yao, H.-C., Yang, R.-Y., 2023. Experimental and numerical study of a barge-type floating offshore wind turbine under a mooring line failure. *Ocean Eng.* 278, 114411.
- Tomasicchio, G.R., Vicinanza, D., Belloli, M., Lugli, C., Latham, J.-P., Iglesias Rodriguez, J.G., Jensen, B., Vire, A., Monbaliu, J., Taruffi, F., et al., 2020. Physical Model Tests on Spar Buoy for Offshore Floating Wind Energy Conversion.
- Tran, T.T., Meuris, B.J., Chartrand, C., Davidson, J., Andersen, J., Eskilsson, C., Kramer, M.B., Papadakis, G., Nielsen, K., 2024. High-fidelity numerical wave tank verification & validation study: wave generation through paddle motion. In: Innovations in Renewable Energies Offshore. CRC Press, pp. 227–236.
- Ullah, Z., Muhammad, N., Choi, D.-H., 2021. On the importance of nonlinear hydrostatic stiffness of offshore floating wind turbine platforms. *Appl. Ocean Res.* 113, 102730.
- Uzunoglu, E., Soares, C.G., 2019. A system for the hydrodynamic design of tension leg platforms of floating wind turbines. *Ocean Eng.* 171, 78–92.
- van Vondelen, A. A.W., Navalakar, S.T., Iliopoulos, A., van der Hek, D.C., van Wingerden, J.W., 2022. Damping identification of offshore wind turbines using operational modal analysis: a review. *Wind Energy Sci.* 7 (1), 161–184.
- Wang, H., Ran, Q., Ma, G., Wen, J., Zhang, J., Zhou, S., 2025a. Optimization design of floating offshore wind turbine mooring system based on DNN and NSGA-III. *Ocean Eng.* 316, 119915.
- Wang, H., Wen, J., Ma, G., Yuan, L., Ran, Q., Zhang, J., Zhou, S., 2025b. Coupled dynamics analysis of floating wind turbine mooring system under extreme operating gust. *Appl. Ocean Res.* 154, 104333.
- Wang, Y., Chen, H.-C., Koop, A., Vaz, G., 2022. Hydrodynamic response of a FOWT semi-submersible under regular waves using CFD: verification and validation. *Ocean Eng.* 258, 111742.
- Wen, X., Yin, G., Liu, T., Ong, M.C., Wang, C., Wang, K., 2025. An optimization framework for mooring design of floating offshore wind turbines using a genetic algorithm based on a surrogate model. *Renew. Energy*, 122807.
- Xi, R., Wang, P., Du, X., Xu, K., Xu, C., Jia, J., 2020. A semi-analytical model of aerodynamic damping for horizontal axis wind turbines and its applications. *Ocean Eng.* 214, 107861.
- Xu, H., Rui, S., Shen, K., Guo, Z., 2023. Investigations on the mooring safety considering the coupling effect of the mooring line snap tension and anchor out-of-plane loading. *Appl. Ocean Res.* 141, 103753.
- Xu, H., Rui, S., Shen, K., Jiang, L., Zhang, H., Teng, L., 2024. Shared mooring systems for offshore floating wind farms: a review. *Energy Rev.* 3 (1), 100063.
- Yang, C., Chen, P., Cheng, Z., Xiao, L., Chen, J., Liu, L., 2023. Aerodynamic damping of a semi-submersible floating wind turbine: an analytical, numerical and experimental study. *Ocean Eng.* 281, 114826.
- Yang, R., Zheng, X., Chen, J., Wu, Y., 2022. Current status and future trends for mooring systems of floating offshore wind turbines. *Sustain. Marine Struct.* 4 (2), 40–54.
- Yu, Z., Ma, Q., Zheng, X., Liao, K., Sun, H., Khayyer, A., 2023. A hybrid numerical model for simulating aero-elastic-hydro-mooring-wake dynamic responses of floating offshore wind turbine. *Ocean Eng.* 268, 113050.
- Zeng, F., Zhang, N., Huang, G., Pan, W., He, M., 2022. An effective bidirectional solving method for the motion and mooring tension of moored floaters. *Ocean Eng.* 259, 111924.
- Zhang, Y., Liu, H., 2023. Coupled dynamic analysis on floating wind farms with shared mooring under complex conditions. *Ocean Eng.* 267, 113323.
- Zhang, Y., Shi, W., Li, D., Li, X., Duan, Y., 2022. Development of a numerical mooring line model for a floating wind turbine based on the vector form intrinsic finite element method. *Ocean Eng.* 253, 111354.

- Zhang, Z., Wang, X., Zhang, X., Zhou, C., Wang, X., 2024. Dynamic responses and mooring line failure analysis of the fully submersible platform for floating wind turbine under typhoon. *Eng. Struct.* 301, 117334.
- Zhang, Z., Yang, H., Wang, R., Zhang, K., Zhou, D., Zhu, H., Zhang, P., Han, Z., Cao, Y., Tu, J., 2025. Effects of combined platform rotation and pitch motions on aerodynamic loading and wake recovery of a single-point moored twin-rotor floating wind turbine. *Energy* , 135137.
- Zhong, W., Zhao, W., Wan, D., Zhao, Y., 2024. Comparison study on mooring line models for hydrodynamic performances of floating offshore wind turbines. *Ocean Eng.* 296, 117083.